Simulations of edge localised mode instabilities in MAST-U Super-X tokamak plasmas

S.F. Smith[1,2], S.J.P. Pamela[2], A. Fil[2], M. Hölzl[3], G.T.A. Huijsmans[4,5], A. Kirk[2], D. Moulton[2], O. Myatra[1,2], A.J. Thornton[2], H.R. Wilson[1,2]

[1] *York Plasma Institute, Department of Physics, University of York, York, UK.*
[2] *CCFE, Culham Science Centre, Abingdon, Oxon, UK.*
[3] *Max-Planck-Institute for Plasmaphysics, EURATOM Association, Garching, Germany.*
[4] *CEA, IRFM, F-13108 Saint-Paul-lez-Durance, France.*
[5] *Eindhoven University of Technology, Eindhoven, The Netherlands*

ABSTRACT

The high heat fluxes to the divertor during edge localised mode (ELM) instabilities have to be reduced for a sustainable future tokamak reactor. A solution to reduce the heat fluxes could be the Super-X divertor, which will be tested on MAST-U. ELM simulations for MAST-U Super-X tokamak plasmas have been obtained, using JOREK. A factor 10 decrease in the peak heat flux to the outer target and almost a factor 8 decrease in the ELM energy fluence when comparing the Super-X to a conventional divertor configuration has been found. A detached MAST-U case, after the roll-over in the target parallel electron density flux, is used as a starting point for ELM burn-through simulations. The plasma burns through the neutrals front during the ELM causing the divertor plasma to re-attach. After the crash a transition back to detachment is indicated, where the recovery to pre-ELM divertor conditions occurs in a few milliseconds, when the neutral pressure is high in the divertor. Recovery times are shorter than the inter-ELM phase in previous MAST experiments. The peak ELM energy fluence obtained after the ELM burn-through is 0.82 kJ/m^2, which is significantly lower than that predicted from the empirical scaling of the ELM energy fluence - indicating promising results for future MAST-U operations.

1 Introduction

High confinement mode (H-mode) [1] is the favoured operation regime for tokamaks, due to the increased core plasma pressure, in comparison to low confinement mode (L-mode). However, as the plasma edge pressure gradient and current density reach critical limits, explosive behaviour is observed; these magneto-hydrodynamic (MHD) instabilities are called edge localised modes (ELMs) and are quasi-periodic [2]. When an ELM occurs the steep pressure pedestal that has built up in the plasma edge collapses and large amounts of energy and particles are released on material surfaces

facing the plasma. ELMs can remove up to 10% of the plasma thermal energy in less than 1 `ms` [3]. Experimentally ELMs are observed as filamentary structures, which erupt from the plasma edge [4, 5], transporting heat and particles to the plasma facing components of a tokamak. Whilst the heat fluxes to the divertor are high, ELMs are useful to regulate impurities within the core plasma through the evacuation of density.

In order to achieve its goal of Q=10 (Q is the ratio of fusion power to plasma heating power) ITER will operate in H-mode. The ELM predictions made for this future tokamak, indicate heat fluxes from type-I ELMs would damage the Tungsten divertor plates [6]. For DEMO, even the steady heat flux is a concern and so it is of great importance that an improved understanding of ELM physics is achieved to ensure durability of divertor materials [7]. In order to reduce ELM heat fluxes various control mechanisms are being explored to obtain suppression or mitigation including RMPs, pellets and kicks [8–12]. However, alternative exhaust geometries are also being researched to reduce the heat fluxes incident on divertor targets.

The MAST-U tokamak will test a new divertor configuration, the Super-X [13, 14], as a possible solution to lower the target heat fluxes. Additional poloidal field coils have been installed, to direct the plasma into the Super-X divertor(s) and to allow control of the strike point radius length (R_s). At larger R_s the contact area of the plasma increases, which decreases the target heat flux. In addition, flux expansion in the chamber is also possible increasing the neutral interaction volume before the plasma reaches the targets [15]. The divertor is closed with a baffle, this design allows for retention of neutrals [15], which is important for attaining detachment whilst keeping impurities low in the core plasma. The detachment process allows for an increase in the radiated energy of the plasma before it reaches the targets; it occurs when there is a significant decrease in plasma density flux, temperature and heat flux to the divertor targets. Operating in a detached regime will be beneficial, especially in future tokamaks, ITER already plans to operate in a partially detached regime [16]. Detachment can be achieved by increasing the upstream plasma density [17] or by increasing radiative losses through an impurity seeding ramp, which leads to an increase in recycling in the divertor and an increase in neutral density at the targets, where atomic processes play a key role.

Plasma detachment has been predicted, for some MAST-U L-mode [18] and H-mode [19] plasmas. However, the behaviour during ELMy H-mode is unknown and so it is of interest to study the characteristics of ELMs in the new Super-X divertor geometry. In this paper we present first simulations of ELMs in MAST-U, in advance of its operation; for this the JOREK code [20, 21] is used. JOREK is a 3D nonlinear MHD code, which is being actively validated against current experiments, including studies of MAST [22]. An overview of the model, used for the simulations, is given in section 2.

Section 3 explores the ELM dynamics of the MAST-U Super-X tokamak focusing on the heat fluxes to the divertor targets and the ELM energy fluence. A direct comparison of the new Super-X divertor is made to a conventional MAST-U divertor configuration where the initial plasma profiles are consistent and the only difference is the outer leg lengths. Section 4 includes simulation results

using the JOREK diffusive neutrals model with separate ion and electron temperature equations. A roll-over is obtained for the MAST-U case, indicating a large neutral density in the Super-X divertor. A comparison of JOREK to SOLPS simulations has been made, given in appendix A, for an L-mode MAST case and a H-mode MAST-U case, to evaluate the ability of such a simplified fluid neutrals model to describe detachment. In section 4 a detached divertor case is then used as a start for the ELM burn-through study. The role of neutrals in the divertor and the extent of the burn-through is simulated along with calculations of ELM recovery times. The simulations in this paper indicate that during an ELM the plasma will burn through the cloud of neutrals, which has built up in the divertor, and the recovery times are found to be smaller than the inter-ELM period. However, the simulations also indicate that the Super-X geometry, and additionally the detached pre-ELM divertor, lead to a considerable buffering of divertor heat fluxes and a deviation from the Eich scaling.

2 The JOREK code adapted for divertor recycling and ELM burn-through

2.1 Numerical model

A reduced two-temperature fluid model with neutrals has been used. It is implemented in JOREK where the seven-field model has variables ψ (poloidal magnetic flux), Φ (electric potential), $v_{\parallel}$ (parallel velocity), ρ (plasma density), T_i (ion temperature), T_e (electron temperature) and ρ_n (neutral density). The reduction assumes that the perpendicular velocity is in the poloidal plane and that the toroidal magnetic field is constant in time. Hence the total plasma velocity ($\vec{v}_{tot}$) and total magnetic field ($\vec{B}$) are given as

$$\vec{v}_{tot} = \vec{v}_{\parallel} + \vec{v}_{\perp} = v_{\parallel}\vec{B} + \vec{e}_{\phi} \times \nabla\Phi, \tag{1}$$

and

$$\vec{B} = \vec{B}_{\phi} + \vec{B}_p = \frac{F_o}{R}\vec{e}_{\phi} + \frac{1}{R}\nabla\psi \times \vec{e}_{\phi}. \tag{2}$$

Where R is the major radius, $\vec{e}_{\phi}$ is the toroidal unit vector and $F_0 = B_0 R_0$, where B_0 is the amplitude of the magnetic field at the magnetic axis ($R = R_0$). Substituting the expressions for the total plasma velocity and total magnetic field projections into the visco-resistive MHD equations gives the reduced model [23]. The set of normalised equations are given by Eq. 3-9, with two projections for the velocity in the perpendicular and parallel directions.

$$\rho\frac{d\vec{v}_E}{dt} = -\nabla_{\perp}p + \vec{J} \times \vec{B} + \mu\nabla^2\left(\vec{v}_E\right) + \mu_{hyp}\nabla^4\vec{v}_E + \left(\rho\rho_n S_{ion} - \rho^2\alpha_{rec}\right)\vec{v}_E, \tag{3}$$

$$\rho\frac{d\vec{v}_{\parallel}}{dt} = -\rho\vec{v}_{\parallel} \cdot \nabla\vec{v}_{\parallel} - \nabla_{\parallel}p + \mu\nabla^2\left(\vec{v}_{\parallel} - V_{NBI}\right) + \mu_{hyp}\nabla^4\vec{v}_{\parallel} + \left(\rho^2\alpha_{rec} - \rho\rho_n S_{ion}\right)\vec{v}_{\parallel}, \tag{4}$$

where the convective derivative is defined as $\frac{d}{dt} = \frac{\partial}{\partial t} + \vec{v}_E \cdot \nabla$

3

$$\frac{\partial \psi}{\partial t} = \eta \left(j - j_A \right) + R \left[\psi, \Phi \right] - \frac{\partial \Phi}{\partial \phi} + \eta_{hyp} \nabla^2 j, \tag{5}$$

$$\frac{\partial \rho}{\partial t} = -\nabla \cdot \left(\rho \left[\vec{v}_\parallel + \vec{v}_E \right] \right) + \nabla \cdot \left(D_\perp \nabla_\perp \rho \right) + S_\rho + D_{hyp} \nabla^4 \rho + \left(\rho \rho_n S_{ion} - \rho^2 \alpha_{rec} \right), \tag{6}$$

$$\frac{\partial (\rho T_i)}{\partial t} = -\rho \vec{v}_E \cdot \nabla T_i - \gamma p_i \nabla \cdot \vec{v}_E + \nabla \cdot \left(\kappa_{\perp i} \nabla_\perp T_i + \kappa_{\parallel i} \nabla_\parallel T_i \right) + S_{T_i}, \tag{7}$$

$$\rho \frac{\partial (\rho T_e)}{\partial t} = -\rho \vec{v}_E \cdot \nabla T_e - \gamma p_e \nabla \cdot \vec{v}_E + \nabla \cdot \left(\kappa_{\perp e} \nabla_\perp T_e + \kappa_{\parallel e} \nabla_\parallel T_e \right)$$
$$+ S_{T_e} - \xi_{ion} \rho \rho_n S_{ion} - \rho \rho_n L_{lines} - \rho^2 L_{brem}, \tag{8}$$

$$\frac{\partial \rho_n}{\partial t} = \nabla \cdot \left(\vec{D}_n : \nabla \rho_n \right) + S_{\rho_n} - \left(\rho \rho_n S_{ion} - \rho^2 \alpha_{rec} \right). \tag{9}$$

Where the parallel current is

$$j = -R^2 \nabla \phi \cdot J = \Delta^* \psi, \tag{10}$$

where $\Delta^* \psi = R^2 \nabla \cdot \left(\frac{\nabla \psi}{R^2} \right)$ is the Grad-Shafranov operator.

The toroidal vorticity W and plasma pressure p are

$$W = \nabla \phi \cdot (\nabla \times v_\perp) = \nabla_\perp^2 \Phi, \tag{11}$$

$$p = \rho(T_i + T_e). \tag{12}$$

The perpendicular gradient is $\nabla_\perp = \nabla - \nabla_\parallel$ where $\nabla_\parallel = \vec{b} \left[\vec{b} \cdot \nabla \right]$ and $\vec{b} = \frac{1}{|B|} \vec{B}$. The Poisson brackets are defined as $[\alpha, \beta] = \vec{e}_\phi \cdot (\nabla \alpha \times \nabla \beta)$. S_ρ, S_T, S_{ρ_n} and j_A are the density, temperature, neutral density and current sources respectively. V_{NBI} is a toroidal momentum source accounting for neutral beam injection. The equations are normalised to the core density ρ_0 and the magnetic permeability μ_0 in order to have a near Alfvén time for the normalised time, where $t_{SI} = t \cdot \sqrt{\mu_0 \rho_0}$. The normalised density, pressure and toroidal current density are $\rho_{SI} = \rho \rho_0$, $p_{SI} = \rho T / \mu_0$ and $j_{SI} = -j/(R\mu_0)$ respectively.

Temperature-dependant Spitzer resistivity ($\eta = \eta_0 \left(T_e/T_{e,0} \right)^{-\frac{3}{2}}$) and viscosity ($\mu = \mu_0 \left(T_e/T_{e,0} \right)^{-\frac{3}{2}}$) are used, where $T_{e,0}$ is the electron temperature at the magnetic axis. The Braginskii parallel thermal conductivities $\kappa_{\parallel e,i}$ are equivalent to $\kappa_\parallel = \kappa_{\parallel 0} \left(T/T_0 \right)^{\frac{5}{2}}$ for electrons and ions. Hyper-diffusive coefficients are also used for numerical stability but are kept low enough not to affect the physics. Profiles are used to represent the H-mode transport barrier; the perpendicular diffusivity for density ($D_\perp$) and temperature ($\kappa_\perp$) are given as radial profiles, which dip in the pedestal region - these are ad hoc values representing anomalous transport.

Equation 9, for the neutral density, describes the fluid neutrals with a diffusive coefficient D_n. The neutrals model has been used previously for MGI and disruption simulations in JOREK [24].

The neutral density only consists of Deuterium atoms - Deuterium molecules and impurities such as carbon from the MAST-U wall are not included, meaning the dissociation process is also not included. Some atomic processes are included in the model - ionisation (S_{ion}) and recombination (α_{rec}) rates, taken from [25] and [26] respectively and the normalised ionisation energy (ξ_{ion}) for Deuterium, are included. The line (L_{lines}) and bremsstrahlung (L_{brem}) radiation rate coefficients are computed using ADAS data [27]. However, the charge exchange process, which leads to momentum losses, is not included. Charge exchange is the dominant atomic process at low temperatures around $1 - 10$ eV, which are relevant divertor temperatures for detachment. Results indicate that charge exchange is not important to obtain a roll-over for detachment but does play a role in the detachment process [28]. Missing physics could be included in future work, including extra species or the charge exchange process. However, this requires additional variables and equations, which will further increase the computational time. The multi-mode ELM simulation shown in this paper already requires approximately three million core hours to run on the MARCONI-Cineca supercomputer, which is why this simpler model has first been tested for the ELM burn-through simulations presented here.

Dirichlet boundary conditions are used for the magnetic field. Where the boundary of the computational domain coincides with a flux surface, Dirichlet boundary conditions are applied. For boundaries with which the flux is incident, such as the targets, there are free outflow boundary conditions for the density and temperature, in the model without neutrals. In the neutrals model the density is reflected back as neutrals as described below. Bohm and sheath boundary conditions are implemented for the parallel velocity where the magnetic flux is not parallel to the boundary. This is to represent the sheath at the boundary, which forces the parallel velocity to equal the sound speed (c_s);

$$\vec{\mathrm{v}}_{tot} \cdot \vec{n} = \pm c_s = \pm \sqrt{\gamma T} \vec{b} \cdot \vec{n}, \tag{13}$$

and

$$nT\vec{\mathrm{v}}_{\parallel} + \kappa_{\parallel}\nabla_{\parallel}T = \gamma_{sh}nT\vec{\mathrm{v}}_{\parallel} \tag{14}$$

where T is T_e or T_i, $\vec{n}$ is the unit vector normal to the boundary, $\gamma = 5/3$ and $\gamma_{sh} = 4.5$ for the sheath boundary conditions. Reflective boundary conditions are implemented for the neutral density; as the plasma density is incident on the boundary this is reflected away as diffusive neutrals. This can be represented by

$$D_n\nabla\rho_n \cdot \vec{n} = -\xi_{re}\rho\vec{\mathrm{v}}_{\parallel} \cdot \vec{n}, \tag{15}$$

where ξ_{re} is the reflective coefficient that determines the source of neutrals from the boundary.

2.2 MAST-U equilibria and simulation set-up

The MAST-U equilibrium is generated with an extended outer leg, using the Fiesta code [29, 30]. $B_T = 0.64$ T, the plasma current is 1 MA, $q_{axis} = 1.1$, $q_{95} = 7.9$ and the central density and sum of the electron and ion temperatures are 0.52×10^{20} m^{-3} and 1.8 keV respectively. The temperature and density profiles are based on MAST pulse 24763 and are unstable to the peeling-ballooning

modes that drive ELMs. The Grad-Shafranov equation is solved again within JOREK for the magnetic flux and a grid is built. To account for the bootstrap current an additional perturbation to the parallel current at the plasma edge is implemented, in the future a more realistic current profile can be obtained using the wide set of diagnostics available on MAST-U. The JOREK grid is a set of 2D Bezier finite elements in poloidal plane (R,Z) and is flux aligned to capture fast parallel transport, until just few `cm` outside the separatrix. Patches are then added to extend the grid to the MAST-U wall [31], such that the wall boundary conditions are represented correctly. A Fourier decomposition is used in the toroidal direction due to the periodicity allowing for investigations into single toroidal mode numbers with the benefit of reduced computational time.

The initial equilibria for each of the MAST-U cases have the same profiles, with the only difference being the outer leg length; each of the cases are given in Fig. 1 a)-e) where the flux contours are shown. Starting from a conventional case Fig. 1 a) where the strike point is at $R_s = 0.7$ `m` to the Super-X case in Fig. 1 d) and a Super-X case with expanded flux in Fig. 1 e), which have strike points at $R_s = 1.5$ `m`. Fig. 1 f) shows the normalised pressure profile, normalised current density profile and the q-profile, used in the simulations, the normalisation of the quantities in JOREK are given in [24]. Fig. 1 g) shows the equilibrium density and temperature profiles as a function of normalised poloidal flux (ψ_n).

Once the equilibrium and MAST-U grid have been obtained the simulation is first run with equilibrium flows only (n=0). Firstly, this allows the Bohm boundary conditions to diffuse from the boundary and secondly it allows the recycling of neutrals from the wall. For the ELM study a quasi-steady state first has to be reached then a perturbation can be introduced, in the form of single/multiple toroidal mode numbers, to seed the ELM. The initial perturbation is much smaller than the equilibrium fields, typically at the level of numerical noise. This initial perturbation only increases if the equilibrium is unstable. When the nonlinear phase of the simulation is reached an ELM crash occurs and a saturation phase follows.

3 ELM simulations: single temperature model without neutrals

Prior to the inclusion of separate energy equations for ions and electrons and the terms related to neutrals, the reduced visco-resistive MHD model was used, here the neutral density equation (and neutral terms) are not included and there is just one energy equation describing both the ion and electron temperatures; $T_i = T_e$.

3.1 Linear parameter scans (Super-X configuration)

In the following, linear simulations of the Super-X case without expanded flux, are performed (Fig. 1 d)). The new MAST-U Super-X equilibrium parameter scans are carried out to observe behaviour of the instability growth rate. Single toroidal mode number (n) simulations are performed for the Super-X case; the growth rates are plotted as a function of n in Fig. 2 a). The growth rate increases with increasing toroidal mode number and plateaus at higher n as expected. Here, diamagnetic
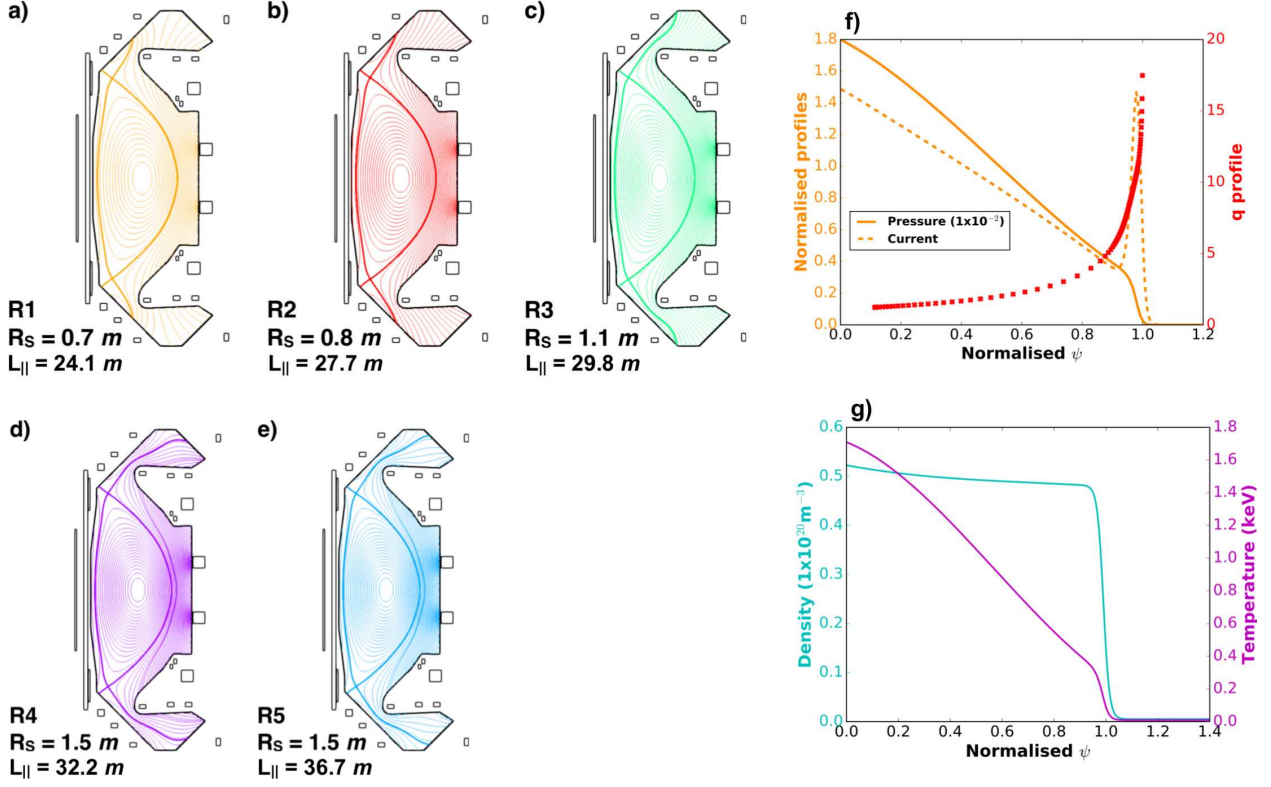
Figure 1: *Poloidal plane flux contour plots for a conventional MAST-U divertor a) extending the outer leg b) and c) towards a Super-X divertor. The Super-X configuration d) with no flux expansion in the divertor chambers and e) with flux expansion. The black boxes indicate the coil positions and the thicker coloured lines show each separatrix. R_s is the strike point radius and $L_\parallel$ is the connection length from midplane to target at $\psi_n = 1.0001$. f) The profiles for pressure, current density and q as a function of ψ_n. g) The density and temperature profiles as a function of ψ_n.*

terms are not included and so high n modes are not suppressed. The following simulations in this section have a single toroidal mode number of $n = 20$. Simulations that include additional mode numbers are more accurate, used later in section 4, although there are limits with regards to the computational resources.

The energy and density pedestal losses are observed for each toroidal mode number. Here, the lower mode numbers result in smaller density and energy losses from the pedestal, which in this case is defined from $\psi_n = 0.9$ to $\psi_n = 1.0$. The losses from the $n = 5$ single mode number case have a factor of 3.5 difference in the pedestal density loss and a factor 10 difference in the energy pedestal losses compared to the $n = 25$ single mode number case. The total energy loss also increases with increasing mode number.

A scan of the resistivity and viscosity are shown in Fig. 2 b) and c) respectively, this is conducted to show the influence of the non-ideal MHD parameters on the stability of the modes. The resistivity follows a resistive ballooning mode regime, where at high resistivity the growth rate increases; at lower resistivity the growth rate appears to saturate. The viscosity has the opposite effect damping the growth rates at higher viscosity, as expected.
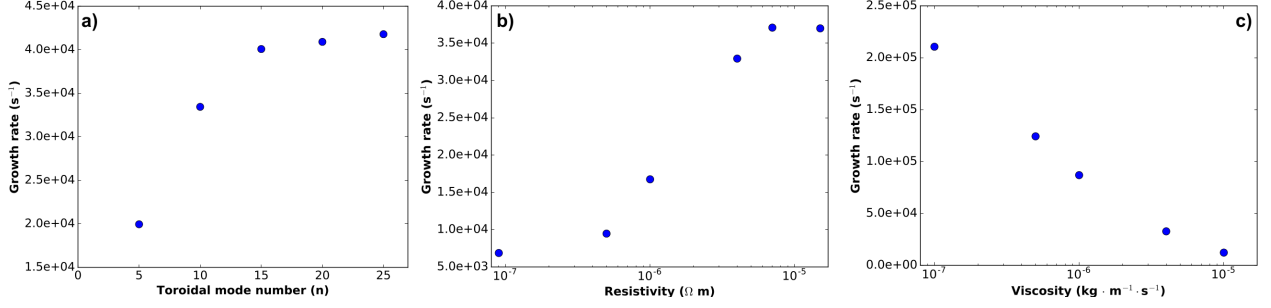
Figure 2: *Linear growth rate of the instability as a function of a) toroidal mode number with a resistivity of 5.4×10^{-6} $\Omega.m$ and a dynamic viscosity of 3.7×10^{-6} $kg.m^{-1}.s^{-1}$. b) Resistivity scan with $n = 20$ and dynamic viscosity of 1.5×10^{-6} $kg.m^{-1}.s^{-1}$. c) Viscosity scan with $n = 20$ and a resistivity of 1.0×10^{-5} $\Omega.m$.*

3.2   Nonlinear ELM dynamics (Super-X R4 configuration)

A nonlinear simulation is performed for the Super-X case, to explore the ELM crash. The MHD parameters used are as follows; the resistivity $\eta = 5.4 \times 10^{-6}$ $\Omega.m$ (a factor 200 above the Spitzer value) and perpendicular/ parallel viscosities $\mu_\perp = 3.7 \times 10^{-6}$ $kg.m^{-1}.s^{-1}$/ $\mu_\parallel = 3.7 \times 10^{-5}$ $kg.m^{-1}.s^{-1}$ respectively. The hyper-resistivity and hyper-viscosity are set to $\eta_{num} = \mu_{num} = 7.0 \times 10^{-15}$ for numerical stability. Perpendicular particle and heat diffusivity profiles are used to represent the transport barrier with values of $D_\perp = 1.5$ $m^2 s^{-1}$ in the core, $D_\perp = 0.5 \times 10^{-2}$ $m^2 s^{-1}$ at $\psi_n = 1.0$ and $\kappa_\perp = 1.9 \times 10^{-8}$ $kg.m^{-1}.s^{-1}$ at the pedestal top. The parallel heat transport coefficient for ions and electrons is combined in the single temperature model, where $\kappa_\parallel = 1.5 \times 10^2$ $kg.m^{-1}.s^{-1}$ (a factor 6 smaller than the Braginskii value for electrons and factor 5 larger than the value for ions).

The evolution of the energy of the modes is shown in Fig. 3 a) for the equilibrium ($n = 0$) and perturbation ($n = 20$) magnetic and kinetic energies. The growth rate of the instability is 3.45×10^4 s^{-1} and the crash occurs at around 1.4 ms. The pressure profile evolution is shown in Fig. 3 b); the time step for each corresponding pressure profile is shown in Fig. 3 a). The pressure starts with a steep pedestal and as the ELM crash occurs the pedestal collapses transporting energy and particles from the core to the open field lines of the SOL and to the divertor regions.

The evolution of the density filaments in the poloidal plane is shown in Fig.3 c), starting from the equilibrium with large density gradient in the edge to when the crash occurs and filaments erupt from the plasma edge. These filaments are small, sheared and slowly rotate with the $E \times B$ rotation due to the ELM. Without a rotation profile the filaments travel much further into the SOL as seen in [22].

When the ELM crash occurs the energy and particle losses in the pedestal are 11% and 13% respectively. The pedestal losses are calculated using volume integrals from $\psi_n = 0.9$ to $\psi_n = 1.0$. The peak heat fluxes to the inner and outer targets are 1.6 MW/m^2 and 0.8 MW/m^2 respectively. The evolution of the heat flux to the lower outer target is shown in Fig. 5 d). The peak heat flux is an order of magnitude lower in comparison to a MAST conventional divertor case. The heat flux
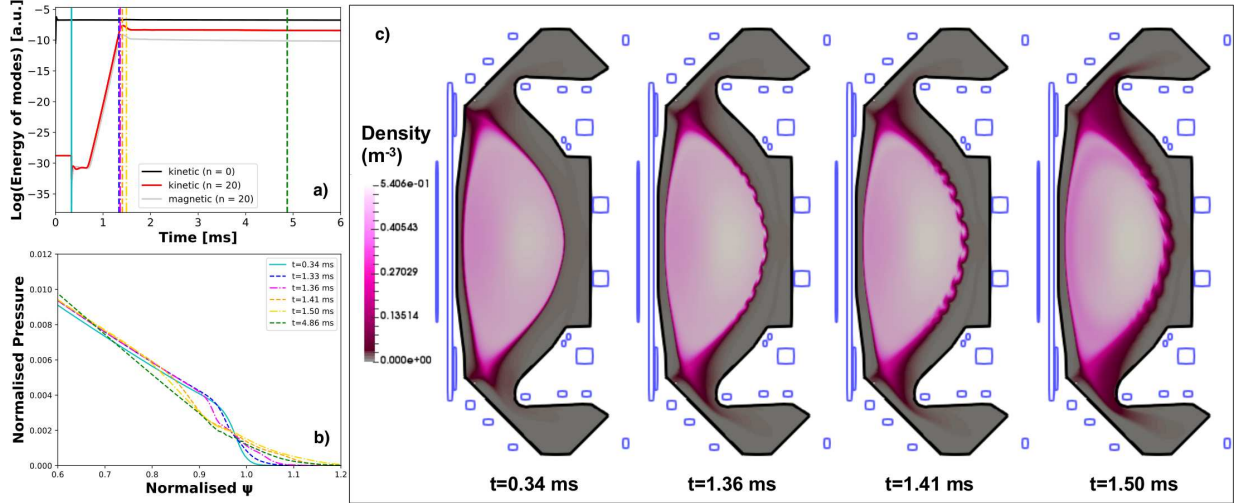
Figure 3: *a) Evolution of the energy of the modes. b) The evolution of the pressure profile. c) Density filament evolution during the crash.*

is also lower than the estimates made due to the target area increase; note that previous ELM simulations for JET [32] using this model produced slightly lower target heat fluxes in comparison to experimental data. The peak target heat fluxes to the upper divertor are 1.3 $\mathtt{MW/m^2}$ (inner) and 0.8 $\mathtt{MW/m^2}$ (outer).

A test is conducted for different transport coefficients for the Super-X, to determine if the assumed diffusivities are causing lower than expected peak heat fluxes. Due to the Super-X outer target having a larger connection length, in comparison to the conventional target, the plasma ejected during an ELM takes longer to reach the target; because of this the choice of diffusive parameters is explored. A scan of the MHD diffusivities is performed and the corresponding peak heat flux to the divertor, due to the ELM, is obtained. When the perpendicular particle diffusivity is varied over two orders of magnitude the growth rate of the instability increases slightly with increasing $D_\perp$. The peak heat flux to the outer Super-X target varies by 0.32 $\mathtt{MW/m^2}$ and decreases with increasing $D_\perp$. The perpendicular thermal conductivity is also varied over two orders of magnitude, resulting in the growth rate of the instability slightly decreasing with increasing $\kappa_\perp$. The peak heat flux varies by 0.46 $\mathtt{MW/m^2}$ over two orders of magnitude, again decreasing with increasing $\kappa_\perp$. The parallel heat diffusivity ($\kappa_\parallel$) is also reduced resulting in the peak heat flux to the outer target arriving later. The peak heat flux varies by 0.4 $\mathtt{MW/m^2}$ over one order of magnitude change in $\kappa_\parallel$. The perpendicular and parallel diffusivities have an effect and are important for the SOL diffusion of parallel heat flux. The results indicate that the choice of the MHD parameters for particle and heat diffusivity is not the reason for the lower than expected heat flux; however, the parameter choice does have an affect on the simulation results.

3.3 MAST-U divertor configuration comparison

In order to verify the above MAST-U simulations and to compare the Super-X to other configurations a scan in the leg length is conducted, using the 5 cases shown in Fig. 1. For the rest of the

paper these cases may be referred to as R1-R5 represented by the different divertor configurations in Fig. 1 a)-e), where R_s the lower outer target strike point radius, is at 0.75, 0.8, 1.1, 1.5, 1.5 m respectively. The connection length ($L_{\parallel}$) is defined from the target to the midplane at $\psi_n = 1.0001$, $L_{\parallel} = 24.1, 27.7, 29.8, 32.2, 36.7$ m for the cases R1-R5 respectively. Each case starts with the same equilibrium, the only difference is the leg length to the outer target. An ELM simulation is run for each case with a single $n = 20$ mode number. The instability growth rates are very similar for each of the cases as is expected for the same equilibrium profiles; with a mean of 3.38×10^4 s^{-1} and standard deviation of 9.8×10^1 s^{-1}. The pedestal particle and energy losses due to the ELM are also very similar; the mean percentage pedestal particle loss is 12.8% with a standard deviation of 0.75%, the mean percentage energy pedestal loss is 10.4% with a standard deviation of 0.49%. The pedestal losses approximately correspond to 0.8 kJ and 1.1×10^{19} particles for each of the cases.
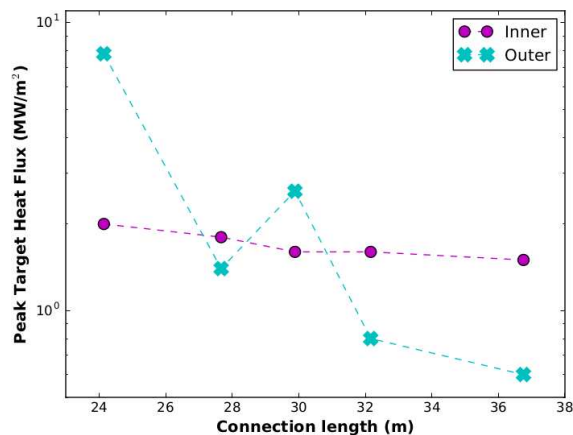

Figure 4: *The peak target heat flux for the inner and outer lower divertor as a function of $L_{\parallel}$.*

Fig. 4 shows the peak heat flux, to the lower inner and outer targets, as a function $L_{\parallel}$. The peak heat flux to the lower inner divertor in each case is similar, however, the peak heat flux to the lower outer target is an order of magnitude less for the Super-X divertor configuration (R4 and R5) in comparison to the conventional case (R1). The simulations show transitioning from a conventional case to the Super-X case reduces the peak heat fluxes by a factor 10 from 8 MW/m^2 to 0.8 MW/m^2. This can be understood by considering the area the heat flux is incident on in both cases - approximately 0.14 m^2 in the conventional case to 1.5 m^2 in the Super-X case. The comparison between R1 and R4 divertor configurations appears to be reasonable considering the change in target area. However, the peak heat fluxes are in general smaller than expected in comparison to target heat fluxes from ELMs in previous MAST experiments [33].

The R3 case, at $L_{\parallel} = 29.8$ m has a higher peak heat flux than R2 ($L_{\parallel} = 27.7$ m), which has a shorter connection length and R_s. It is thought that the angle of incidence plays an important role here, the field lines are almost perpendicular to the target in the R3 case, this is not the case for R2. The target flux is also less expanded in the R3 case, as seen in Fig. 5, in comparison to R2. However, it appears the flux expansion has a less significant role in reducing the ELM peak heat fluxes to the outer target than the angle of incidence, as seen in Fig. 4 by comparing the peak heat
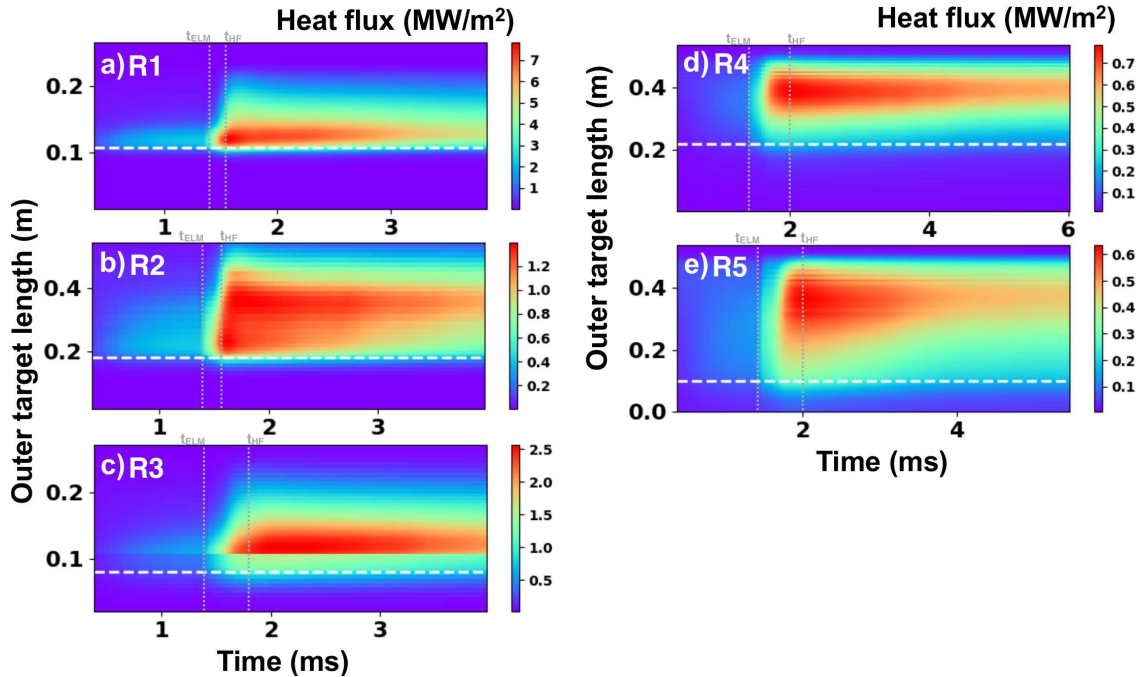
flux of R4 with R5 and R2 with R3.

Figure 5: *Heat flux patterns onto the outer target for R1-R5 shown in a)-e) respectively. The horizontal white dashed line indicates the position of the separatrix. The vertical grey dotted lines indicate the time the ELM crash occurs (the peak in MHD activity) and the time the peak heat flux occurs. Note the different length, time and heat flux scales in each heat flux pattern.*

Fig. 5 shows the evolution of the heat flux onto the outer target in each case R1-R5 corresponding to Fig. 5 a)-e) respectively. The white dashed line indicates the separatrix position. In all the cases the ELM occurs around 1.4 `ms`. It is seen that for the cases R1 and R2 the peak heat flux to the outer target then occurs approximately 0.1 `ms` after the crash. When moving further out to the R3 case the peak heat flux occurs 0.4 `ms` after the crash and is further delayed to 0.6 `ms` after the ELM crash in the R4 and R5 Super-X cases. The heat flux patterns are continuous in the length along the target except for the R3 case (Fig. 5 c)), which has a discontinuity at around 0.1 `m`; the reason for this is that the strike point is positioned very close to where one of the corners of the Super-X divertor chamber is located - further indicating the angle of incidence is important.

The parallel energy fluence ($\varepsilon_{||}$) is calculated for each of the divertor configurations. $\varepsilon_{||}$ is calculated by integrating the parallel heat flux $q_{||}$ for the duration of the ELM, defined by Eich et al. [6] as

$$\varepsilon_{||}(s) = \int_{t_{\mathrm{ELM}}} \alpha_B q_{||}(s,t)\mathrm{d}t \tag{16}$$

where α_B is the angle between the magnetic field lines and the divertor target and s is the distance along the target.

Fig. 6 a) shows profiles of $\varepsilon_{||}$ as a function of the target distance for each of the divertor configurations, where the separatrix position is given by the black dashed line. $\varepsilon_{||}$ is largest for the conventional divertor configuration (R1) and is spread over a narrower target distance. As with

the peak heat flux, R3 has a higher peak $\varepsilon_\parallel$ than R2. However, it is seen $\varepsilon_\parallel$ is spread further over the target, also note α_B is smaller for the R2 configuration. The peak $\varepsilon_\parallel$ for the Super-X configurations, with (R5) and without (R4) expanded flux, are approximately a factor 8 lower than $\varepsilon_\parallel$ for R1 and the spread along the target is observed.
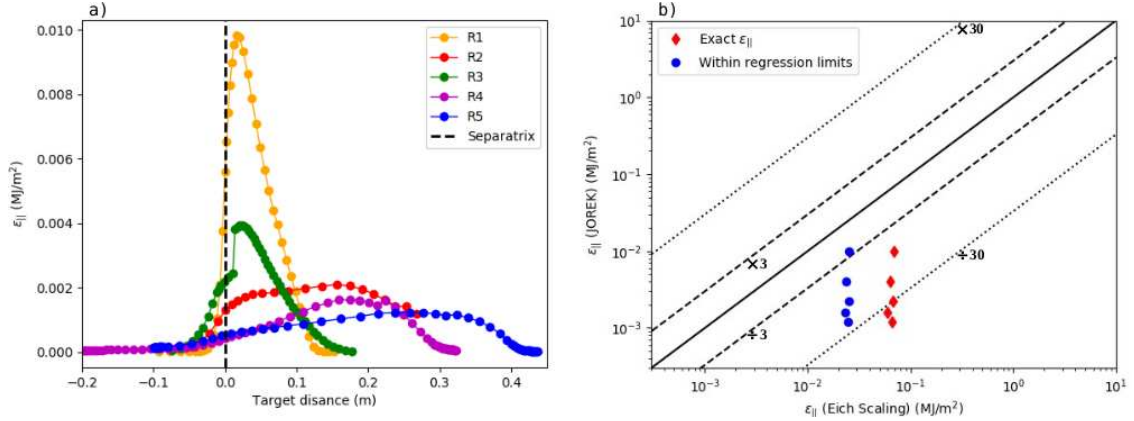

Figure 6: *a) Profiles of the ELM energy fluence ($\varepsilon_\parallel$) as a function of target distance for each of the divertor configurations. b) The ELM peak energy fluence in JOREK, for each divertor configuration, compared to the exact scaling ($\varepsilon_\parallel = 0.28 \times n_{e,ped}^{0.75} \times T_{e,ped}^{0.98} \times \Delta W_{ELM}^{0.52} \times R_{geo}^{1.0}$) and within the regression limits ($\varepsilon_\parallel = 0.14 \times n_{e,ped}^{0.9} \times T_{e,ped}^{0.99} \times \Delta W_{ELM}^{0.36} \times R_{geo}^{1.4}$) of the empirical scaling of the ELM parallel energy fluence.*

The empirical scaling of the ELM parallel energy fluence, obtained from experimental data analysis on multiple tokamaks in [6], is used for a comparison to the JOREK simulations for MAST-U. In [6] $\varepsilon_\parallel$ is given as

$$\varepsilon_\parallel(\text{MJ/m}^2) = 0.28 \pm 0.14 \times n_{e,ped}^{0.75 \pm 0.15} \times T_{e,ped}^{0.98 \pm 0.1} \times \Delta W_{ELM}^{0.52 \pm 0.16} \times R_{geo}^{1.0 \pm 0.4} \tag{17}$$

Fig. 6 b) shows $\varepsilon_\parallel$ calculated from the MAST-U simulations for each of the configurations (R1-R5) using Eq. 16 compared against the Eich ELM scaling law Eq. 17. The conventional configuration R1 is the case with the best agreement at around three times the estimate for the exact and at the limit of the scaling law. Note, in [34] some of the JOREK JET cases, also without diamagnetic terms, are close to or just outside three times the estimate. The Super-X cases R4 and R5 appear to deviate from the empirical scaling, for these the parallel energy fluences are above a factor 30 different compared to the exact Eich ELM scaling and just below a factor 30 comparing to the scaling with altered limits.

4 ELM burn-through simulations: two temperature model with neutrals

ELM simulations are now performed with the JOREK diffusive neutrals, two temperature model given in section 2. The extent of the plasma burn-through in the Super-X divertor during an ELM, is investigated. First an attempt to obtain a detached divertor is shown, following this the ELM burn-through results are given. The multi-mode number ELM simulations are constrained by

computational resources, so it has only been possible to simulate multiple toroidal mode numbers of $n = 2, 4, 6, ..., 20$. An attempt to use more mode numbers was unsuccessful, on the MARCONI-Cineca supercomputer. This was due to the memory required for the simulation, partly due to the larger model with more variables, which includes separate equations for the ion and electron temperatures as well as an equation for the neutral density. The effect of divertor neutral pressure, after the ELM crash, is briefly examined.

4.1 Obtaining a detached divertor for ELM burn-through studies.

For the purposes of the ELM burn-through study in the Super-X it is first important to demonstrate detachment, or to at least obtain a high neutral density in the divertor with the JOREK neutrals model. For the R4 equilibrium without expanded flux a scan in upstream density is performed. Six test cases are each run, for 20 `ms`, until a saturated state is reached to allow neutral density to build up in the divertor; the cases have different upstream densities ranging from $0.05 - 0.31 \times 10^{20}$ `m`$^{-3}$. The neutral diffusivity coefficient (D_n) is set to just over 200 `m`^{2}/`s` everywhere; this value is lower than the neutral diffusivity estimated in appendix A.1. The lower D_n can be somewhat justified as lower divertor/target temperatures would be obtained if more physics, such as the missing atomic processes, would be included in the model, and at lower temperatures the neutral diffusivity is lower. Divertor pumping is not included in this case.
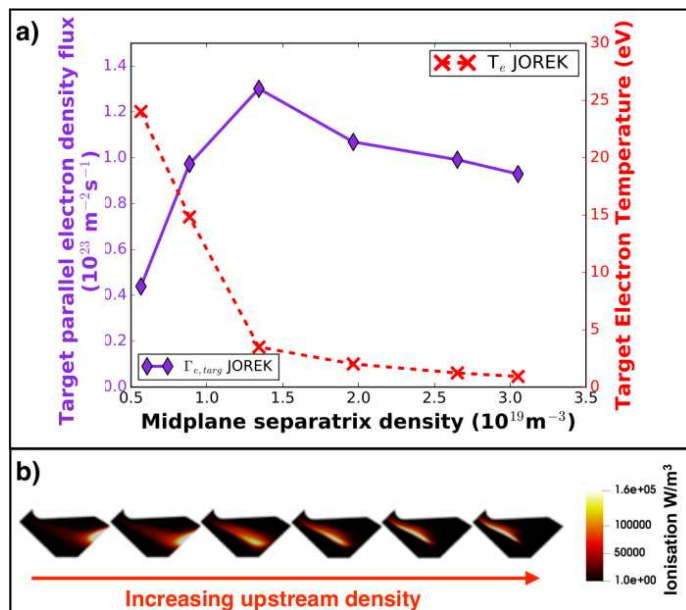

Figure 7: *a) The target parallel electron density flux and target electron temperature (at the separatrix) as a function of upstream density. b) The ionisation in the lower divertor for the R4 scan.*

Fig. 7 a) shows for increasing upstream density a roll-over in the target parallel electron density flux (Γ_e) is observed. As this occurs the target electron temperature decreases below 5 `eV`. The roll-over is not steep but the ionisation front also is seen to move off of the target upstream (Fig. 7 b)) as the roll-over occurs. The case after the roll-over, with mid-plane separatrix density of

13

2.0×10^{19} m^{-3} in Fig. 7 a), is used for the ELM simulations. This case is closest in terms of Γ_e in a comparison to SOLPS results from [19]. A comparison to SOLPS is given in appendix A.3 (Fig. 16). Appendix A also contains a comparison between a JOREK and SOLPS attached L-mode MAST case (in A.2) and comparison of a H-mode MAST-U Super-X case with expanded divertor flux (in A.3). The expanded divertor flux equilibrium is more similar to the SOLPS case given in [19].

The upstream density scan was conducted without divertor pumping; however, MAST-U will have cryopumps in the Super-X divertor to remove impurities and for density control. Pumps are implemented in the simulations as line sinks in the upper and lower outer divertors and a scan of the pumping speed has been obtained with equilibrium flows only. The parameters for these simulations are given in the appendix B. The addition of the pumps modifies the densities and temperatures at the targets, while only slightly affecting the upstream profiles just outside the separatrix. Fig. 8 shows the saturated peak target values to the lower outer target of the Super-X as a function of pumping speed. Whilst the heat flux to the targets is fairly constant for all pumping speeds, the heat flux slightly increases after the target has evolved from a detached to an attached state. The impact of the pump is explored and it is seen that as the pumping speed is increased, the neutrals are being removed from the divertor, leading to a decrease in densities and an increase in electron and ion temperatures. There appears to be a threshold, where the plasma re-attaches - when the neutral pumping is high enough, the neutral density significantly drops at the target along with the plasma density and the peak target electron temperature increases from around 4 `eV` to 40 `eV`, i.e. by a factor 10. This indicates if the pumping in MAST-U is too high at these values of upstream density then the target temperatures could be above those required for a detached state. The results could be on the pessimistic side as the JOREK simulations do not seem to be as deeply detached in comparison to the predictions of what is more likely to be observed experimentally.
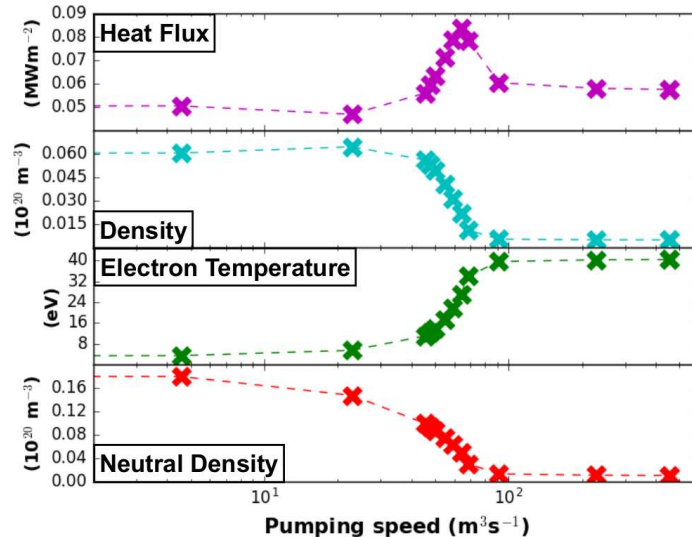

Figure 8: *The saturated peak heat flux, peak density, peak electron temperature and peak neutral density on the outer lower divertor target as a function of pumping speed.*

4.2 Toroidal mode number scan

Before the multiple mode number simulations are presented, a scan of toroidal mode number is obtained to observe the growth rates in the linear phase for the different models. Fig. 9 a) shows the growth rates as a function of toroidal mode number. The blue circles are the scan for the single temperature visco-resistive reduced MHD model. This is compared to the two temperature model (without neutrals) in JOREK and the two temperature model with neutrals, used for the ELM burn-through simulations. The growth rates for the two temperature model are higher than the single temperature model but still follow a similar trend. The toroidal mode number scan for the two temperature model with neutrals indicate that the neutrals suppress the instability growth rate at high toroidal mode number and in this case $n = 10$ is the dominant mode number. Note, diamagnetic terms are not included in the simulations.

A suggestion as to why the neutrals have this effect on the growth rates could be due to the plasma-neutral interactions, causing increased energy damping of higher mode numbers in comparison to the lower mode numbers. The higher mode number perturbations tend to be more localised to the edge of the plasma as shown in Fig. 9 b), where the plasma-neutral interactions occur, which could be damping the energy more strongly. Lower mode number perturbations, on the other hand, tend to spread further into the plasma core and are therefore probably less affected by the plasma-neutral interactions in the edge. The ionisation and line radiation are localised at the outboard side around the edge of the plasma, an example of the ionisation is shown in Fig. 9 c), during the $n = 20$ linear growth phase (the ionisation has the same structure for the other mode number simulations). Both the ionisation and line radiation are slightly higher for the $n = 20$ and $n = 2$ toroidal mode numbers in comparison to the $n = 10$ mode number simulation during the linear growth phase; the ionisation and line radiation are just inside the separatrix, where the peak outboard mid-plane values are both roughly a factor 1.2 higher for the $n = 20$ simulation in comparison to the $n = 10$ simulation. The increase in neutrals altering the instability growth rate is also observed in the reflectivity scan in appendix B.1. The reflective coefficient is changed after a detached divertor case is obtained and then a single mode number ($n = 20$) ELM simulation is performed. Fig. 19 shows the ELM crash occurs later with increasing reflectivity (ie. with an increased number of neutrals in the domain).

4.3 Multi-mode ELM simulation

Multi-mode number simulations are performed ($n = 2, 4, 6, ..., 20$) in an attempt to produce a more realistic ELM crash. An attempt to use more mode numbers was unsuccessful due to the memory required for the simulation. The inclusion of multiple mode numbers leads to a violent crash and more suppressed MHD activity after the ELM in comparison to a single mode number simulation, where the filamentary oscillations are long lived. Single mode number simulations are given in appendix B. As MAST has a high rotation, this simulation includes a rotation profile. The same MHD parameters as the single mode number simulations are used and the reflectivity is set to 95%.
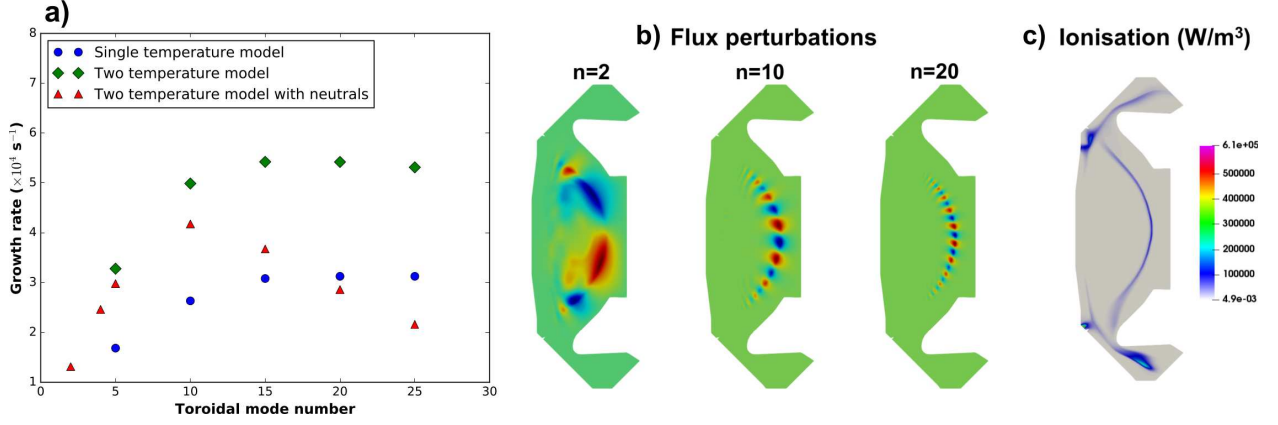
Figure 9: *a) The growth rates as a function of toroidal mode number for the visco-resistive reduced MHD single temperature JOREK model, the two temperature model and the two temperature model with neutrals. b) The flux perturbations during the linear growth phase of the simulations for n=2 (left), n=10 (centre) and n=20 (right). c) The ionisation in the poloidal plane in the linear growth phase of the $n = 20$ simulation.*

After a cold divertor has been obtained $n = 2, 4, 6, 8, 10, 12, 14, 16, 20$ are added to the simulation, the energy of the mode numbers grow, shown in Fig. 10 a) and when the ELM crash occurs $n = 10$ is the dominant mode number, as expected from the growth rates of toroidal mode number scan. The ELM crash leads to increased fluxes to the divertor and burn-through is observed in the Super-X, after the crash recovery times can be calculated and a saturation phase with lower MHD activity occurs.

The evolution of the nonlinear structure of the ELM filaments is observed using the JOREK synthetic fast camera diagnostic, Fig. 10 b). The JOREK fast camera diagnostic code was developed and first used for MAST simulations shown in [22]. This code has now been slightly adapted as the neutral density can be used directly from the simulation data instead of applying a fit, which was previously done. Per image there are 384,000 pixels corresponding to the lines of sight on which the radiation is integrated over, where the photon emissivity coefficient data is given as a function of density and temperature, using ADAS data. The examples of the JOREK fast camera, given in Fig. 10 b) start from a well-confined plasma before the instability occurs (top-left). Filaments then start to form and violently erupt into the scrape-off-layer and start to rotate. The non-linearity of the ELM filaments due to mode interaction is apparent in comparison to the more uniform filament structure of the single mode number simulations (given in appendix B). When the crash occurs an increase in the visible light is then seen in the divertor regions, due to the flux of heat and particles. The visible light in the divertor region is so bright that a filter had to be applied, restricting the maximum light, in order to observe the filaments. After, the filaments start to reduce in size, whilst the divertor remains bright (two lower-right images of Fig. 10 b)).

The violent crash leads a quick burn-through. A simple analytical calculation is performed to determine the extent of the ELM burn-though given the neutral density in the Super-X chamber before the ELM. The neutral density in the lower divertor has been integrated over the volume of the Super-X chamber to determine the number of neutral particles. This is calculated to be
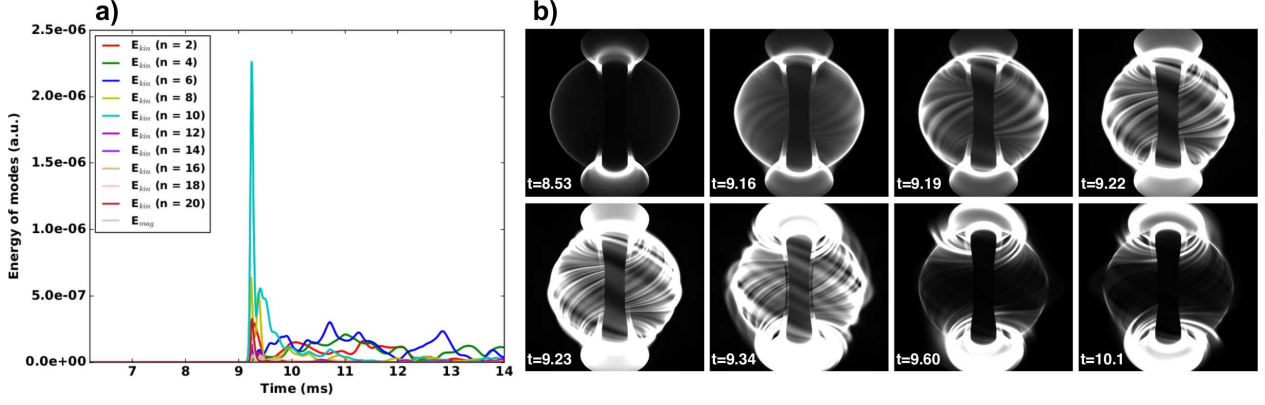
16

Figure 10: *a) The evolution of the kinetic (coloured lines) and magnetic (grey lines) energy of the mode numbers for the multi-mode simulation. b) The evolution of the filamentary structures during the multi-mode ELM simulation imaged with a synthetic fast camera diagnostic (time given in* `ms`*).*

2.98×10^{18} particles, the ionisation energy per neutral particle is 13.6 `eV`. Therefore, it would take 6.5 `J` for all the neutrals in the lower divertor to be ionised. Assuming all the energy lost from the pedestal, during the ELM crash, goes to the divertor regions then 1050 `J` would go to the lower divertor. This simple calculation indicates ELM burn-through will occur unless the ELM size is a factor 160 lower or there is a factor 160 more neutrals in the lower divertor for the ELM to be completely buffered. However, the ELM is partially buffered with the inclusion of neutral particles in the simulations, not only is energy taken from the ELM to ionise the neutrals front in the divertor but as the density flux from the ELM arrives on the target, even more neutrals are being reflected from the wall, and these neutrals also need to be ionised by the ELM energy before it is incident on the target.

The evolution of the peak outer lower target values, of the heat flux, plasma density, electron temperature, and neutral density, are give in Fig. 11 a). The peak heat flux to the outer lower target, due to the ELM, is 9.8 `MW/m`^{2} and is a factor three lower to the upper outer target. The peak heat flux arrives roughly 0.1 `ms` after the ELM crash, and 1.5 `ms` after the crash the heat flux has relaxed to almost pre-ELM conditions. When the evolution of the heat flux is plotted along the target the peak is located just outside the separatrix. The peak in heat flux then rapidly (in around 0.1 ms) moves along the outer target to around 20 cm from the separatrix, before it travels back towards the separatrix with a significantly reduced amplitude. The peak electron temperature on the upper and lower outer targets is 150 `eV` and recovers to below 5 `eV` (almost pre-ELM conditions) around 3 `ms` after the crash.

The density and electron temperature, in the poloidal plane, during the ELM are given in Fig. 11 b) and c) respectively. The density filaments extend further into the SOL and finger-like structures are observed around the X-point and in the divertor region; this is also seen in the electron temperature. Due to the higher density and temperature around the baffle region the peak heat flux onto the baffle is calculated. The peak heat flux is 2 `MW/m`^{2} to the baffle, a factor of 5 lower than the peak heat flux to the outer target of the Super-X. Due to the baffle position it could be

an issue during large ELMs; however, the baffle in MAST-U has been covered with carbon tiles to manage this. The magnetic field structure is plotted to observe whether the finger-like structures are due to the magnetic field. The Poincaré plot in Fig. 11 d) shows the whole region around the strike point is ergodised, with field lines connecting the pedestal top to the target.
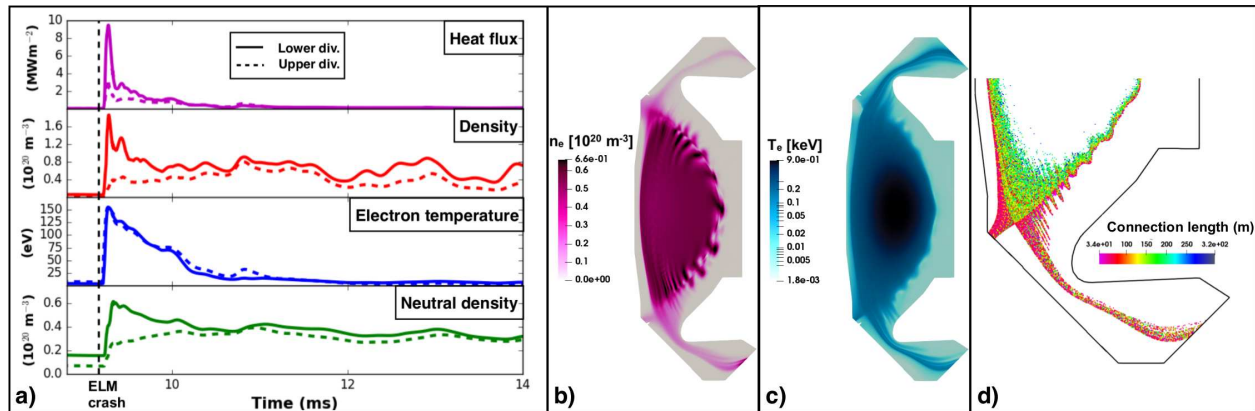

Figure 11: *a) The evolution of the peak outer target values for the heat flux, density, electron temperature and neutral density for the upper (dashed lines) and lower (solid lines) divertors. A poloidal plot of the density b) and electron temperature c) during the ELM. d) Poincaré plot of the magnetic field structure during the ELM.*

In the simulation before the ELM there is a higher plasma and neutral density and lower electron temperature in the lower divertor in comparison to the upper divertor. During the ELM crash the filaments rotate due to the intrinsic $E \times B$ rotation caused by the ELM itself. This rotation leads to a non-symmetric distribution of fluxes to the upper and lower divertors. The simulation results show that more plasma density is diverted to the lower divertor during the ELM than the upper divertor (Fig. 11 a) and b) and 10 b)); because of this there is a larger burn-through observed in the lower divertor and a higher peak heat flux, which is roughly three times more, in the lower divertor (Fig. 11 a)). Consequently, a higher neutral density is observed in the lower divertor, in comparison to the upper divertor, just after the ELM. The peak target electron temperatures, due to the ELM, are the same in both divertors and the recovery time of the target electron temperature to almost pre-ELM conditions is the same. The heat flux recovery times are similar in both divertors (Fig. 11 a)).

The parallel energy fluence, as described in section 3.3 for the different divertor configurations, is analysed. $\varepsilon_{||}$ is analysed firstly to determine if the Super-X extended leg configuration follows the Eich ELM scaling and then to determine whether a detached plasma also follows the scaling law. Fig. 12 shows $\varepsilon_{||}$ as a function of ΔW_{ELM}. For the simulations performed ΔW_{ELM} is the only quantity in Eq. 17 which is different for each simulation. The black dashed line in Fig. 12 shows the Eich ELM scaling and the black circles indicate $\varepsilon_{||}$ as predicted by Eq. 17 for the cases R1-R5 and the Super-X case with neutrals. The R4 JOREK Super-X simulation (without neutrals) given in Fig. 12 shows a deviation of a factor 14 from the scaling. The peak $\varepsilon_{||}$ for the multi-mode R4 simulation with neutrals (orange diamond Fig. 12) is a factor 2 lower than the R4 case using

18

the single temperature model without neutrals (red triangle), despite having over double the ELM energy loss. The results indicate that not only do the extended leg cases deviate from the Eich ELM scale (as seen in Fig. 6) but also a detached plasma causes an even larger deviation from the Eich ELM scale. This deviation is a promising result as $\varepsilon_{||}$ decreases, indicating the ELM could be somewhat buffered if the divertor is in a Super-X configuration and/or a detached regime.
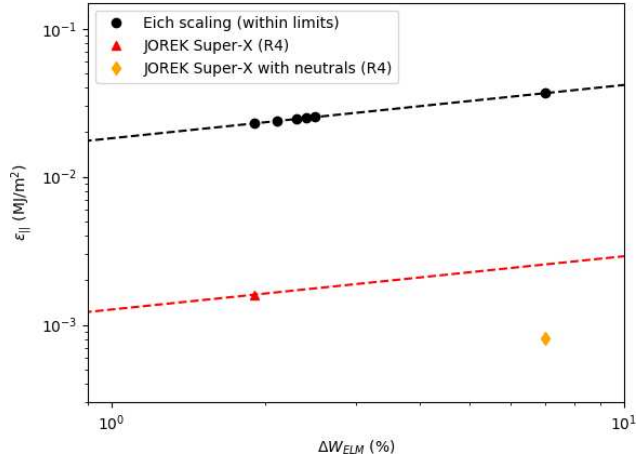

Figure 12: *The peak ELM parallel energy fluence as a function of ELM energy loss. $\varepsilon_{||}$ is significantly lower, than the Eich ELM scaling, for the Super-X detached plasma despite the larger ΔW_{ELM}. $\varepsilon_{||}$ is given for the Eich ELM scaling (black) and for the JOREK Super-X cases with (orange) and without neutrals (red).*

The evolution of the ionisation in the lower outer Super-X divertor, during the ELM simulation, is shown in Fig. 13. Starting from a detached divertor before the ELM at t=8.83 `ms`, as the ELM crash starts at approximately t=9.18 `ms` the ionisation front is still upstream and the divertor is still detached. At approximately t=9.27 `ms` the peak heat flux is incident on the outer divertor targets and the ionisation has significantly increased on and in front of the outer targets, 2 `ms` after the crash the ionisation front is still at the target and the electron temperature is above 10 `eV` for both divertors so it is assumed the plasma is still attached at this point of the simulation. The ionisation decreases almost 1 `ms` after the ELM crash and at 12.4 `ms` the plasma starts to detach in both the upper and lower divertors, the peak electron target temperature has decreased to below 5 `eV` and the ionisation front starts to move off the target, indicating the plasma may detach again after the ELM during the inter-ELM phase. The detached regime is not long lived in the lower divertor due to the MHD activity of the lower toroidal mode numbers and the lower divertor attaches again. At around 13.7 `ms` the lower divertor appears to detach again as the peak target temperature drops again below 5 `eV` and the ionisation front moves upstream. The upper divertor remains detached after 12.4 `ms` but by analysing the ionisation in the divertor it appears that the divertor is not deeply detached after the ELM crash in this multi-mode simulation.

4.4 Neutral pressure role in the Super-X after the ELM crash (pumping scan)

Due to the larger than expected MHD activity after the ELM, an artificial elimination of the mode numbers is implemented for a divertor pumping scan. Only the $n = 0$ equilibrium mode is kept
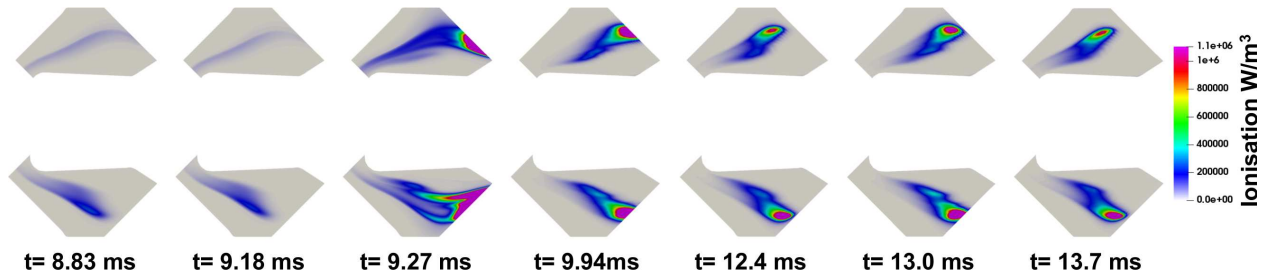
19

Figure 13: *The evolution of the ionisation in the upper and lower outer Super-X divertors during the ELM simulation.*

to eradicate the MHD activity after the ELM. In an attempt to replicate the inter-ELM phase this abrupt blocking of the mode numbers could be acceptable. In the future, equilibria could be constructed from experimental data, which could improve the accuracy of the simulations and diamagnetic terms would be expected to suppress after-ELM activity. Sources are included to further reproduce the behaviour of the inter-ELM phase, to allow the density and temperature profiles to build back to the equilibrium profiles used at the start of the simulation. The source allows the profiles to fill up for around 20 ms, which is a typical inter-ELM phase observed in previous MAST experiments [35].

When the finite mode numbers are removed at 10.2 `ms`, after the energy of the $n = 10$ mode number has decreased, a scan in divertor pumping is conducted. The pumps are again included in the upper and lower divertors as neutral sinks and the simulations are continued until a saturated state is reached several milliseconds later. The evolution of the peak target values in the lower divertor are analysed. The results indicate that the Super-X divertor detachment occurs quickly, less than 2 `ms`, after the ELM crash - this time period is a fraction of the time of the inter-ELM phase. For the highest pumping speeds the temperatures rise again and the plasma re-attaches. The peak target electron temperature again saturates at around 40 `eV`.

A comparison is made for the upper and lower divertors with pumping after the ELM. There is a shift in the thresholds for the upper and lower divertors re-attaching; this occurs at a lower pumping amplitude for the upper divertor in comparison to the lower divertor, due to the increased densities in the lower divertor. The lower target saturated quantities as a function of pumping speed have the same thresholds for detachment and saturation as the equilibrium pumping scan, before the ELM, given in Fig. 8.

5 Conclusions

ELM simulations for the MAST-U Super-X configuration have been explored. The single temperature visco-resistive reduced MHD simulations without neutrals indicate there is a factor 10 reduction in the peak heat flux to the outer target of the Super-X in comparison to a conventional divertor configuration, which is reasonable considering the increase in area from the conventional to Super-X targets.

A roll-over in the target parallel electron density flux for the MAST-U H-mode case is obtained.

As the divertor detaches the target electron temperature drops below 5 eV and the ionisation front moves upstream. A detached case after the roll-over is used as a starting point for the ELM burn-through simulations. More relevant equilibria have been used for comparisons to SOLPS for a MAST L-mode case and a MAST-U H-mode case.

ELM burn-through simulations have been obtained for single and multiple toroidal mode numbers with the neutrals model. It is seen that $n = 10$ is the dominant mode number, where it is thought higher mode number energies, which are more localised in the plasma edge, are damped due to the plasma-neutral interactions. The multi-mode number simulation performed gives a peak ELM heat flux of $\sim$9.5 MW/m^2 at the lower Super-X target. The plasma appears to detach around 3 ms after the ELM, indicating the potential for the plasma to detach in the inter-ELM phase of large ELMs on MAST-U. However, in the lower divertor the plasma is not as deeply detached as before the ELM due to the MHD activity after the ELM in this simulation. Due to the $E \times B$ rotation the differences in the upper and lower divertor have been observed during the ELM crash, where a larger ELM burn-through in the lower divertor occurs, resulting in higher peak heat fluxes.

The ELM energy fluence for MAST-U has been investigated. The conventional divertor case shows agreement of $\varepsilon_{||}$ to the Eich ELM scaling law but the Super-X extended leg configurations differ. However, whilst $\varepsilon_{||}$ deviates from the scaling, it is significantly lower for the Super-X cases. The results suggest the scaling may have to be adapted for extended leg divertors and for detached plasmas, but are promising as they indicate Super-X detached plasmas will have decreased ELM energy fluences.

Divertor pumping simulations are explored, pumping speed scans are obtained before and after the ELM, which indicate the same threshold. Specifically, when the pumping speed is increased above a threshold the plasma appears to not detach - which should be taken into consideration when the MAST-U cryopumps are in operation. The threshold could be expected to increase in the experiment due to the missing physics in this model, where it becomes difficult to simulate deeply detached plasmas.

When MAST-U starts operation in the near future questions about the behaviour during ELMy H-mode in the Super-X configuration can be answered, until then the simulations presented here can provide useful guidance. The ELM simulations with the neutrals model show the plasma burn-through the neutrals front in the Super-X divertor. Recovery times to pre-ELM conditions in the divertor are on the order of a few milliseconds in each case where the neutral density in the divertor is high enough. The recovery times are shorter than the inter-ELM phase for large ELMs in previous MAST experiments; indicating promising results with regards to future experiments on the MAST-U Super-X tokamak.

Acknowledgement

References

[1] F. Wagner, G. Becker, K. Behringer, D. Campbell, A. Eberhagen, W. Engelhardt, G. Fussmann, O. Gehre, J. Gernhardt, G. v. Gierke, G. Haas, M. Huang, F. Karger, M. Keilhacker, O. Klüber, M. Kornherr, K. Lackner, G. Lisitano, G. G. Lister, H. M. Mayer, D. Meisel, E. R. Müller, H. Murmann, H. Niedermeyer, W. Poschenrieder, H. Rapp, H. Röhr, F. Schneider, G. Siller, E. Speth, A. Stäbler, K. H. Steuer, G. Venus, O. Vollmer, and Z. Yü. Regime of Improved Confinement and High Beta in Neutral-Beam-Heated Divertor Discharges of the ASDEX Tokamak. *Physical Review Letters*, 49(19):1408–1412, 11 1982. ISSN 0031-9007. doi: 10.1103/PhysRevLett.49.1408. URL https://link.aps.org/doi/10.1103/PhysRevLett.49.1408.

[2] A. W. Leonard. Edge-localized-modes in tokamaks. *Physics of Plasmas*, 21(9):090501, 9 2014. ISSN 1070-664X. doi: 10.1063/1.4894742. URL http://aip.scitation.org/doi/10.1063/1.4894742.

[3] H Zohm. Edge localized modes (ELMs). *Plasma Physics and Controlled Fusion*, 38(2):105–128, 2 1996. ISSN 0741-3335. doi: 10.1088/0741-3335/38/2/001. URL http://stacks.iop.org/0741-3335/38/i=2/a=001?key=crossref.f28892e44e8eadadb5c7b755b5fc53e6.

[4] A. Kirk, B. Koch, R. Scannell, H. R. Wilson, G. Counsell, J. Dowling, A. Herrmann, R. Martin, M. Walsh, and M. Walsh. Evolution of Filament Structures during Edge-Localized Modes in the MAST Tokamak. *Physical Review Letters*, 96(18):185001, 5 2006. ISSN 0031-9007. doi: 10.1103/PhysRevLett.96.185001. URL https://link.aps.org/doi/10.1103/PhysRevLett.96.185001.

[5] T. Eich, A. Herrmann, and J. Neuhauser. Nonaxisymmetric energy deposition pattern on asdex upgrade divertor target plates during type-i edge-localized modes. *Physical Review Letters*, 91(19), 2003. ISSN 10797114. doi: 10.1103/PhysRevLett.91.195003.

[6] T. Eich, B. Sieglin, A.J. Thornton, M. Faitsch, A. Kirk, A. Herrmann, and W. Suttrop. ELM divertor peak energy fluence scaling to ITER with data from JET, MAST and AS-

DEX upgrade. *Nuclear Materials and Energy*, 12:84–90, 8 2017. ISSN 2352-1791. doi: 10. 1016/J.NME.2017.04.014. URL https://www.sciencedirect.com/science/article/pii/ S2352179116302927.

[7] R.A. Pitts, S. Carpentier, F. Escourbiac, T. Hirai, V. Komarov, S. Lisgo, A.S. Kukushkin, A. Loarte, M. Merola, A. Sashala Naik, R. Mitteau, M. Sugihara, B. Bazylev, and P.C. Stangeby. A full tungsten divertor for ITER: Physics issues and design status. *Journal of Nuclear Materials*, 438:S48–S56, 7 2013. ISSN 0022-3115. doi: 10.1016/J.JNUCMAT.2013.01.008. URL https://www.sciencedirect.com/science/article/pii/S0022311513000160.

[8] T.E. Evans, M.E. Fenstermacher, R.A. Moyer, T.H. Osborne, J.G. Watkins, P. Gohil, I. Joseph, M.J. Schaffer, L.R. Baylor, M. Bécoulet, J.A. Boedo, K.H. Burrell, J.S. deGrassie, K.H. Finken, T. Jernigan, M.W. Jakubowski, C.J. Lasnier, M. Lehnen, A.W. Leonard, J. Lonnroth, E. Nardon, V. Parail, O. Schmitz, B. Unterberg, and W.P. West. RMP ELM suppression in DIII-D plasmas with ITER similar shapes and collisionalities. *Nuclear Fusion*, 48(2):024002, 2 2008. ISSN 0029-5515. doi: 10.1088/0029-5515/48/2/024002. URL http://stacks.iop. org/0029-5515/48/i=2/a=024002?key=crossref.5fc036c755d01774a135b54ca469ab4d.

[9] A. Kirk, J. Harrison, Yueqiang Liu, E. Nardon, I. T. Chapman, P. Denner, and P. Denner. Observation of Lobes near the X Point in Resonant Magnetic Perturbation Experiments on MAST. *Physical Review Letters*, 108(25):255003, 6 2012. ISSN 0031-9007. doi: 10.1103/PhysRevLett. 108.255003. URL https://link.aps.org/doi/10.1103/PhysRevLett.108.255003.

[10] L. R. Baylor, N. Commaux, T. C. Jernigan, N. H. Brooks, S. K. Combs, T. E. Evans, M. E. Fenstermacher, R. C. Isler, C. J. Lasnier, S. J. Meitner, R. A. Moyer, T. H. Osborne, P. B. Parks, P. B. Snyder, E. J. Strait, E. A. Unterberg, and A. Loarte. Reduction of Edge-Localized Mode Intensity Using High-Repetition-Rate Pellet Injection in Tokamak H -Mode Plasmas. *Physical Review Letters*, 110(24):245001, 6 2013. ISSN 0031-9007. doi: 10.1103/PhysRevLett. 110.245001. URL https://link.aps.org/doi/10.1103/PhysRevLett.110.245001.

[11] P.T. Lang, A. Burckhart, M. Bernert, L. Casali, R. Fischer, O. Kardaun, G. Kocsis, M. Maraschek, A. Mlynek, B. Plöckl, M. Reich, F. Ryter, J. Schweinzer, B. Sieglin, W. Suttrop, T. Szepesi, G. Tardini, E. Wolfrum, D. Zasche, H. Zohm, and The ASDEX Upgrade Team. ELM pacing and high-density operation using pellet injection in the ASDEX Upgrade all-metal-wall tokamak. *Nuclear Fusion*, 54(8):083009, 8 2014. ISSN 0029-5515. doi: 10.1088/0029-5515/54/8/083009. URL http://stacks.iop.org/0029-5515/54/i=8/a= 083009?key=crossref.77725514ee77e5036fcd9e9402257da2.

[12] E. de la Luna, I.T. Chapman, F. Rimini, P.J. Lomas, G. Saibene, F. Koechl, R. Sartori, S. Saarelma, R. Albanese, J. Flanagan, F. Maviglia, V. Parail, A.C.C. Sips, E.R. Solano, and JET contributors. Understanding the physics of ELM pacing via vertical kicks in JET in view of ITER. *Nuclear Fusion*, 56(2):026001, 2 2016. ISSN 0029-5515. doi: 10.1088/0029-5515/ 56/2/026001. URL http://stacks.iop.org/0029-5515/56/i=2/a=026001?key=crossref. 85c756c11c43ed3c452cd5b8a2c025ae.

[13] G. Fishpool, J. Canik, G. Cunningham, J. Harrison, I. Katramados, A. Kirk, M. Kovari,

H. Meyer, and R. Scannell. MAST-upgrade divertor facility and assessing performance of long-legged divertors. *Journal of Nuclear Materials*, 438(SUPPL), 2013. ISSN 00223115. doi: 10.1016/j.jnucmat.2013.01.067.

[14] P. M. Valanju, M. Kotschenreuther, S. M. Mahajan, and J. Canik. Super-X divertors and high power density fusion devices. In *Physics of Plasmas*, volume 16, 2009. doi: 10.1063/1.3110984.

[15] I. Katramados, G. Fishpool, M. Fursdon, G. Whitfield, V. Thompson, and H. Meyer. MAST upgrade closed pumped divertor design and analysis. *Fusion Engineering and Design*, 86(9-11):1595–1598, 10 2011. ISSN 0920-3796. doi: 10.1016/J.FUSENGDES.2011.02.060. URL https://www.sciencedirect.com/science/article/pii/S0920379611002304.

[16] A.S. Kukushkin, H.D. Pacher, and R.A. Pitts. Characteristics of divertor detachment for ITER conditions. *Journal of Nuclear Materials*, 463:586–590, 8 2015. ISSN 0022-3115. doi: 10.1016/J.JNUCMAT.2014.10.042. URL https://www.sciencedirect.com/science/article/pii/S0022311514007260.

[17] C.S. Pitcher, A.W. Carlson, C. Fuchs, A. Herrmann, W. Suttrop, J. Schweinzer, and M. Weinlich. Routes to divertor detachment in ASDEX Upgrade. *Journal of Nuclear Materials*, 241-243:696–700, 2 1997. ISSN 0022-3115. doi: 10.1016/S0022-3115(97)80124-9. URL https://www.sciencedirect.com/science/article/pii/S0022311597801249.

[18] E Havlíčková, J Harrison, B Lipschultz, G Fishpool, A Kirk, A Thornton, M Wischmeier, S Elmore, and S Allan. SOLPS analysis of the MAST-U divertor with the effect of heating power and pumping on the access to detachment in the Super-x configuration. *Plasma Physics and Controlled Fusion*, 57(11):115001, 11 2015. ISSN 0741-3335. doi: 10.1088/0741-3335/57/11/115001. URL http://stacks.iop.org/0741-3335/57/i=11/a=115001?key=crossref.1189ca7b2936d4104038cb5efefc0dfb.

[19] D Moulton, B Lipschultz, and J Harrison. Detachment onset in MAST-U according to SOLPS-ITER. 44th EPS Conference on Plasma Physics, O5.129, 2017. URL http://ocs.ciemat.es/EPS2017PAP/pdf/O5.129.pdf.

[20] G.T.A Huysmans and O Czarny. MHD stability in X-point geometry: simulation of ELMs. *Nuclear Fusion*, 47(7):659–666, 7 2007. ISSN 0029-5515. doi: 10.1088/0029-5515/47/7/016. URL http://stacks.iop.org/0029-5515/47/i=7/a=016?key=crossref.54c4a396297481f3a5413a556faf8695.

[21] Olivier Czarny and Guido Huysmans. Bézier surfaces and finite elements for MHD simulations. *Journal of Computational Physics*, 227(16):7423–7445, 8 2008. ISSN 0021-9991. doi: 10.1016/J.JCP.2008.04.001. URL https://www.sciencedirect.com/science/article/pii/S0021999108002118?via%3Dihub.

[22] S J P Pamela, G T A Huijsmans, A Kirk, I T Chapman, J R Harrison, R Scannell, A J Thornton, M Becoulet, F Orain, and the MAST Team. Resistive MHD simulation of edge-localized-modes for double-null discharges in the MAST device. *Plasma Physics and Controlled Fusion*, 55(9):095001, 9 2013. ISSN 0741-3335. doi: 10.1088/0741-3335/

55/9/095001. URL http://stacks.iop.org/0741-3335/55/i=9/a=095001?key=crossref.83196737dfcd53f0452e0edd91a0b417.

[23] H. R. Strauss. Nonlinear, three-dimensional magnetohydrodynamics of noncircular tokamaks. *Physics of Fluids*, 19(1):134, 8 1976. ISSN 00319171. doi: 10.1063/1.861310. URL https://aip.scitation.org/doi/10.1063/1.861310.

[24] A. Fil, E. Nardon, M. Hoelzl, G. T. A Huijsmans, F. Orain, M. Becoulet, P. Beyer, G. Dif-Pradalier, R. Guirlet, H. R. Koslowski, M. Lehnen, J. Morales, S. Pamela, C. Passeron, C. Reux, F. Saint-Laurent, and JET Contributors. Three-dimensional non-linear magnetohydrodynamic modeling of massive gas injection triggered disruptions in JET. *Physics of Plasmas*, 22(6):062509, 6 2015. ISSN 1070-664X. doi: 10.1063/1.4922846. URL http://aip.scitation.org/doi/10.1063/1.4922846.

[25] G.S. Voronov. A Practical Fit Formula for Ionization Rate Coefficients of Atoms and Ions by Electron Impact:Z= 1–28. *Atomic Data and Nuclear Data Tables*, 65(1):1–35, 1 1997. doi: 10.1006/ADND.1997.0732. URL https://www.sciencedirect.com/science/article/pii/S0092640X97907324.

[26] Richard H. Huddlestone and Stanley L. Leonard. Plasma Diagnostic Techniques. *Plasma Diagnostic Techniques. Edited by Richard H. Huddlestone and Stanley L. Leonard. Library of Congress Catalog Card Number 65-22763. Published by Academic Press, New York, 1965.*, 1965. URL http://adsabs.harvard.edu/abs/1965pdt..conf.....H.

[27] H. P. Summers. http://www.adas.ac.uk/, Atomic Data and Analysis Structure User Manual. URL http://www.adas.ac.uk/.

[28] B D Dudson, J Allen, T Body, B Chapman, C Lau, L Townley, D Moulton, J Harrison, and B Lipschultz. The role of particle, energy and momentum losses in 1D simulations of divertor detachment. *Plasma Physics and Controlled Fusion*, 61(6):065008, 6 2019. ISSN 0741-3335. doi: 10.1088/1361-6587/ab1321. URL https://iopscience.iop.org/article/10.1088/1361-6587/ab1321.

[29] G. Cunningham. High performance plasma vertical position control system for upgraded MAST. *Fusion Engineering and Design*, 2013. ISSN 09203796. doi: 10.1016/j.fusengdes.2013.10.001.

[30] L. Pangione, G. McArdle, and J. Storrs. New magnetic real time shape control for MAST. *Fusion Engineering and Design*, 88(6-8):1087–1090, 10 2013. ISSN 0920-3796. doi: 10.1016/J.FUSENGDES.2013.01.048. URL https://www.sciencedirect.com/science/article/pii/S0920379613000586.

[31] S. Pamela, G. Huijsmans, A.J. Thornton, A. Kirk, S.F. Smith, M. Hoelzl, and T. Eich. A wall-aligned grid generator for non-linear simulations of MHD instabilities in tokamak plasmas. *Computer Physics Communications*, 243:41–50, 10 2019. ISSN 0010-4655. doi: 10.1016/J.CPC.2019.05.007. URL https://www.sciencedirect.com/science/article/pii/S0010465519301560.

[32] S J P Pamela, G T A Huysmans, M N A Beurskens, S Devaux, T Eich, S Benkadda,

and JET EFDA contributors. Nonlinear MHD simulations of edge-localized-modes in JET. *Plasma Physics and Controlled Fusion*, 53(5):054014, 5 2011. ISSN 0741-3335. doi: 10.1088/ 0741-3335/53/5/054014. URL http://stacks.iop.org/0741-3335/53/i=5/a=054014?key= crossref.212d2d2c35beb4c0e9d3bc715e550114.

[33] A. J. Thornton, A. Kirk, I. T. Chapman, and J. R. Harrison. Divertor heat fluxes and profiles during mitigated and unmitigated edge localised modes (ELMs) on the Mega Amp Spherical Tokamak (MAST). *Journal of Nuclear Materials*, 438(SUPPL), 2013. ISSN 00223115. doi: 10.1016/j.jnucmat.2013.01.026.

[34] S.J.P. Pamela, G.T.A. Huijsmans, T. Eich, S. Saarelma, I. Lupelli, C.F. Maggi, C. Giroud, I.T. Chapman, S.F. Smith, L. Frassinetti, M. Becoulet, M. Hoelzl, F. Orain, S. Futatani, and JET Contributors. Recent progress in the quantitative validation of JOREK simulations of ELMs in JET. *Nuclear Fusion*, 57(7):076006, 7 2017. ISSN 0029-5515. doi: 10.1088/1741-4326/aa6e2a. URL http://stacks.iop.org/0029-5515/57/i=7/a=076006? key=crossref.50842675cc833ce70bba0134ab3e241e.

[35] A Kirk, G F Counsell, H R Wilson, J-W Ahn, R Akers, E R Arends, J Dowling, R Martin, H Meyer, M Hole, M Price, P B Snyder, D Taylor, M J Walsh, Y Yang, and the MAST team. ELM characteristics in MAST. *Plasma Physics and Controlled Fusion*, 46(3):551–572, 3 2004. ISSN 0741-3335. doi: 10.1088/0741-3335/46/3/009. URL http://stacks.iop.org/ 0741-3335/46/i=3/a=009?key=crossref.67a666efd11ce548b75f650b25807b52.

[36] D Hoving. Divertor conditions in non-linear MHD ELM simulations. Technical report, MASTER report, Eindhoven University of Technology, 2009. URL https://pure.tue.nl/ws/ files/46931055/757689-1.pdf.

[37] Xavier BONNIN, Wouter DEKEYSER, Richard PITTS, David COSTER, Serguey VOSKOBOYNIKOV, and Sven WIESEN. Presentation of the New SOLPS-ITER Code Package for Tokamak Plasma Edge Modelling. *Plasma and Fusion Research*, 11(0):1403102– 1403102, 2016. ISSN 1880-6821. doi: 10.1585/pfr.11.1403102. URL https://www.jstage. jst.go.jp/article/pfr/11/0/11_1403102/_article.

[38] S F Smith, SJP Pamela, Aj Thornton, D Moulton, M Hölzl, A Kirk, HR Wilson, and Gta Huijsmans. Numerical simulations of edge localised modes in MAST-U plasmas. 45th EPS Conference on Plasma Physics, P4.1061, 2018. URL http://ocs.ciemat.es/EPS2018PAP/ pdf/P4.1061.pdf.

A   Appendix A - Assessment of the JOREK neutrals model

In the following appendix first the neutral diffusive coefficient is estimated using the formula in [36], before a comparison of the JOREK diffusive neutrals model is made with SOLPS [37]; SOLPS is a widely used SOL transport model. The comparison commences with a simple L-mode MAST case in an attached divertor regime and then a more advanced comparison of a H-mode MAST-U case, where a roll-over in the particle density flux with increasing upstream density has been obtained - this is a characteristic of detachment. The model, described in section 2, including neutrals and the two energy equations has been used to obtain the results given here.

A.1   Calculating the neutral diffusivity

The neutral diffusion coefficient D_n is implemented to describe the motion of neutrals. In the simulations D_n is set to one constant value everywhere in the domain. However, it is unclear what a realistic value of D_n should be; the choice of this parameter has an impact on the simulation results such as target density and temperatures. Nevertheless, a choice can be made which provides comparable results to other codes, that include more physics. A choice of the neutral diffusion coefficient can also be made using an approximation first implemented and used in JOREK by D. Hoving [36]. The implementation of this approximation for these simulations of MAST and MAST-U resulted in numerical instabilities where large gradients in the pressure occur. Therefore, the attempt to include this formula into the two temperature diffusive neutrals model has been so far unsuccessful, but could be considered for future work. Instead, the formula has been used to compare to the choice of D_n. This approximation for the neutral diffusion takes into account charge exchange, which was otherwise neglected in the simulations, where due to the large charge exchange, the thermal speed of the neutrals can be approximated to the thermal speed of the ions. An approximate formula for the neutral diffusion coefficient is (from [36])

$$D_n = \frac{\lambda^2}{\tau} = v_{th}^2 \tau = \frac{N_{d.o.f} k_B T_i}{\rho(<\sigma v>_{c.x.} + <\sigma v>_{ion})}, \tag{18}$$

where λ is the neutral mean free path for collisions, $1/\tau$ is the frequency of collisions, v_{th} is the thermal velocity, $N_{d.o.f}$ is the number of degrees of freedom ($N_{d.o.f} = 3$), k_B is the Boltzmann constant and T_i is the ion temperature, ρ is the plasma density, $<\sigma v>_{ion}$ is the ionisation reaction rate and $<\sigma v>_{c.x.}$ is the charge exchange reaction rate. The normalised JOREK $<\sigma v>_{c.x.}$ and $<\sigma v>_{ion}$ are given as

$$<\sigma v>_{c.x.} = 4.116 \times 10^{-14} \exp\left(-\frac{13.6^{1.1}}{T_e}\right) \cdot \left(\frac{T_e}{6}\right)^{0.15}, \tag{19}$$

and

$$<\sigma v>_{ion} = 0.2917 \times 10^{-13} \left(\frac{13.6}{T_e}\right)^{0.39} \frac{1}{0.232 + \frac{13.6}{T_e}} \exp\left(-\frac{13.6}{T_e}\right). \tag{20}$$

27

An estimation of the neutral diffusivity can be calculated over the domain using the equation for D_n. Examples of the neutral diffusivity values are given in Fig. 14 where D_n has been calculated in a saturated state. Note, D_n is not calculated during the simulations but a constant value for D_n is used everywhere. The examples show a MAST L-mode and a MAST-U Super-X H-mode case, using the density and temperatures given at the end of the simulations in the saturated state, as inputs. D_n ranges from around 6.0×10^2 to 2.4×10^5 $\mathtt{m^2 s^{-1}}$. Typically, in the simulations values of around 300 $\mathtt{m^2 s^{-1}}$ (MAST L-mode attached plasma) and 200 $\mathtt{m^2 s^{-1}}$ (MAST-U H-mode detached plasma) are used, and sensitivity scans have been performed to estimate the extent of the role that D_n plays in the simulations. Lower than estimated values for D_n are used than what are calculated using Eq. 18, justified by the missing physics, which causes higher divertor/target temperatures and at higher temperatures the neutral diffusivity is is higher.
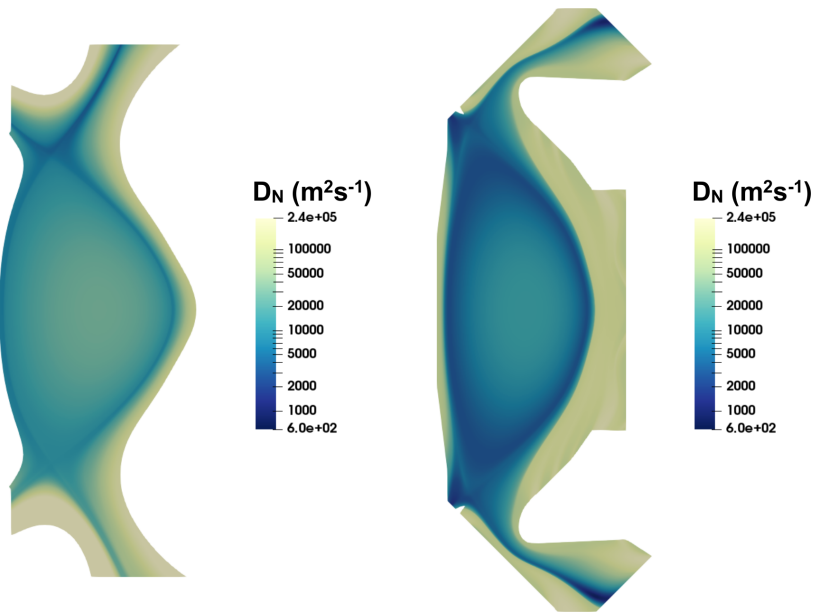

Figure 14: *The amplitude of the diffusive neutral coefficient according to the calculation from Eq. 18, for the MAST L-mode case (left) and the MAST-U Super-X H-mode case (right).*

A.2   L-mode MAST case

The double-null MAST discharge, 30356, is used where the toroidal field is 0.436 $\mathtt{T}$, the plasma current is 0.750 $\mathtt{MA}$, q_{95} is 5.4 and the injected neutral beam power is 2.0 $\mathtt{MW}$. This discharge has a central density of 2.7×10^{19} $\mathtt{m^{-3}}$ and a central electron temperature of 1200 $\mathtt{eV}$.

The same discharge has been previously used for SOLPS simulations given in [18]. The equilibrium density and temperature profiles are fitted to the profiles obtained from Thompson scattering diagnostic data. The neutral reflectivity (ξ_{re}) is set to 100%. The perpendicular particle diffusivity is set to 4 $\mathtt{m^2 s^{-1}}$ everywhere. The neutral diffusivity is set to 300 $\mathtt{m^2 s^{-1}}$. A scan in the neutral diffusivity has been conducted and it is worth noting that this parameter influences the saturated peak target values. Increasing neutral diffusivity increases the plasma and neutral density at the

target, whilst decreasing the ion and electron temperatures. The perpendicular heat diffusivity is 2.5×10^{-8} kg·m^{-1}·s^{-1} inside and 9.7×10^{-9} kg·m^{-1}·s^{-1} outside the separatrix giving a perpendicular heat diffusivity between 0.3 and 10 m^2/s. A pump has been defined along the outboard side of the lower leg of the MAST grid to remove neutrals from the divertor, as in SOLPS.

a) Outer lower target profiles
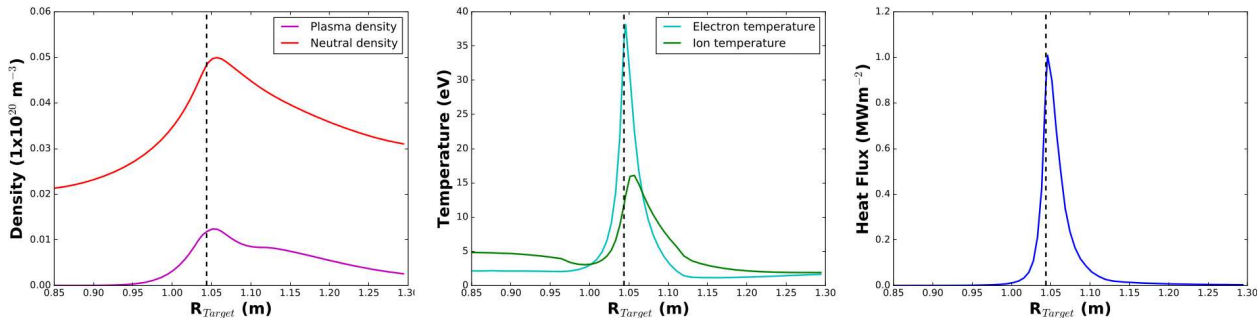
b)

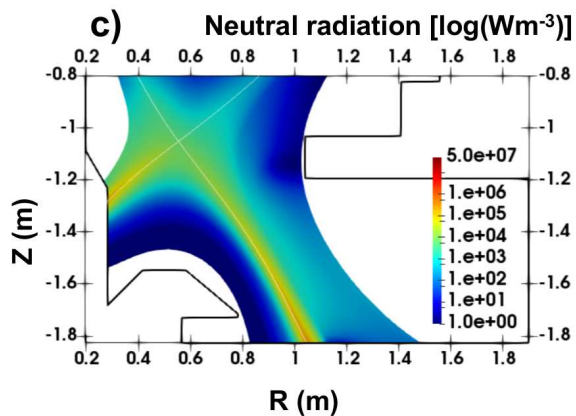| Target Peak	JOREK	SOLPS
Heat Flux (MW/m^2)	1.0	1.5
Density (1×10^{20} m^{-3})	0.01	0.05
Electron Temperature (eV)	37	35
Ion Temperature (eV)	15	20
Neutral Density (1×10^{20} m^{-3})	0.05	0.03

c) Neutral radiation [log(Wm^{-3})]

Figure 15: *a) The plasma density and neutral density (left), electron and ion temperature (centre) and heat flux (right) as a function of major radius at the lower outer target. The black dashed line indicates the separatrix position. b) Table comparing JOREK and SOLPS peak outer target values. c) JOREK neutral line radiation in the lower divertor region, the white line indicates the separatrix.*

The JOREK simulations are performed with equilibrium flows ($n = 0$) only. This allows the influence of the Bohm boundary conditions to diffuse from the wall, along with a diffusion of neutrals from the wall due to the reflective boundary condition. The profiles at the outer lower target are shown in Fig. 15 a), at a quasi-saturated phase around 6 ms. The profiles show similar trends to those given by SOLPS in [18]. The peak values of the outer lower target are less than a few cm outside the separatrix as in SOLPS. The peak in the ion temperature is further into the SOL than the peak in electron temperature; and the electron temperature peak is around 37 eV, too high for a detached regime. The peak values are used for a more direct comparison to SOLPS; these are given in the table in Fig. 15 b). JOREK and SOLPS are in reasonable agreement for the peak target values, but the plasma density is a factor 5 larger in SOLPS. The line radiation from neutral species is shown in Fig. 15 c) and is comparable to that found in previous SOLPS simulations [18]. Similar amplitudes for the neutral line radiation are observed in the divertor region, which peaks

on the target just outside the separatrix and in both cases the plasma is attached. The differences could be due to missing effects in JOREK particularly carbon radiation.

A.3 H-mode MAST-U Super-X case

For the purposes of the ELM burn-through study in the Super-X it is first important to demonstrate detachment, or to at least obtain a high neutral density in the divertor with the JOREK neutrals model. The comparison of the R4 equilibrium is given in Fig. 16. The amplitude of Γ_e is significantly lower in JOREK and the roll-over is not as steep and the target electron temperature is slightly higher in the JOREK case than the SOLPS case. However, the roll-over occurs at roughly the same upstream density in both cases and the target electron temperature drops below 5 eV when the roll-over occurs.
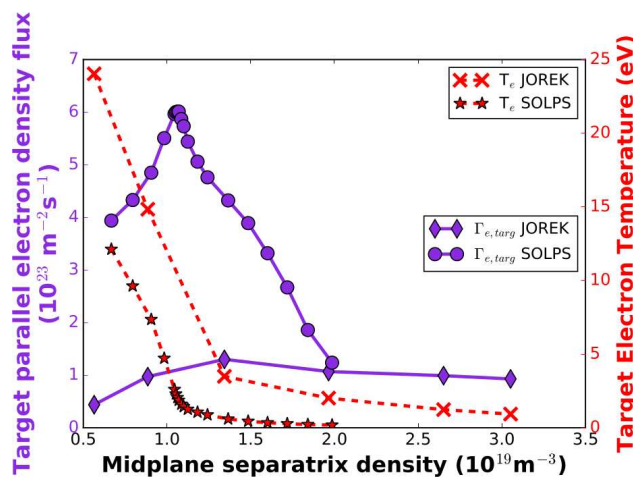

Figure 16: *a) The target parallel electron density flux and target electron temperature as a function of upstream density, comparing JOREK with SOLPS [19] for the R4 scan.*

The R5 equilibrium is compared to the SOLPS case given in [19] as these equilibria are more alike. Five cases are run, where the only difference is the upstream density ranging from $0.2 - 3.1 \times 10^{19}$ m^{-3}. The simulations are run for 30 ms with equilibrium flows to allow neutral density to build up in the divertor and to reach a saturated state. Fig. 17 a) shows that as the mid-plane separatrix density is increased there is a roll-over in the plasma density flux to the outer target, indicating a high neutral density, cold divertor and detachment for the highest upstream density cases. The electron temperature at the target decreases to below a few eV and the ionisation front is seen to move upstream with increasing upstream density, as shown in Fig. 17 b). A comparison has been made to SOLPS, for this MAST-U Super-X H-mode case. The SOLPS results are from [19], where the MAST-U equilibrium with expanded flux is used. In JOREK the perpendicular diffusivity profiles were set to be the same as SOLPS. The comparison shows that the results from JOREK are not as deeply detached as SOLPS, due to the shallow roll-over observed in Fig. 17 a). Divertor pumping in this case was important - when a pump was not included the plasma appeared to be detached even at the lower upstream densities, simulated here, due to the high neutral density
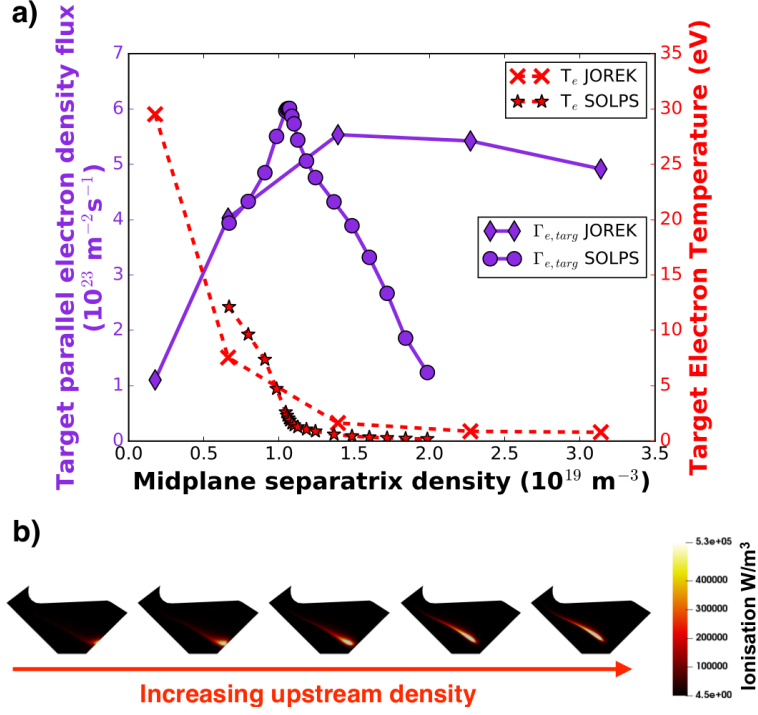
Figure 17: *a) The target parallel electron density flux and target electron temperature as a function of upstream density, comparing JOREK with SOLPS [19] for the R5 scan. b) The ionisation in the lower divertor is shown for the R5 scan from the JOREK simulations.*

in the divertor. In contrast, if the pumping amplitude is too high then the plasma does not detach because of the lack of neutrals and radiative losses in the divertor.

A.4 Summary of comparison

A comparison has been made for a MAST L-mode case to SOLPS, with qualitative agreement for an attached plasma. A MAST-U H-mode case has also been compared to SOLPS simulations where the basic features of detachment are observed with the JOREK fluid neutrals model. A roll-over was observed indicating detachment. However, it is not as steep as SOLPS and this is due to the missing physics from the JOREK model, most likely the charge exchange process leading to momentum losses. Future work could include adapting the model further to include charge exchange as well as a density-temperature dependant neutral diffusivity, and the inclusion of other neutral species such as deuterium molecules and carbon could be important. The inclusion of this extra physics will further increase the computational time of the simulations, some of which already take months to run on the MARCONI-Cineca supercomputer using 44 nodes (48 cores per node). Whilst, the simple diffusive neutrals model does not perfectly replicate SOLPS, for our present purposes of ELM simulations and burn-through the results presented are useful as they demonstrate the model is sufficient to capture the essential features, of the divertor, for the MAST and MAST-U cases.

B   Appendix B - Single mode number ELM burn-through

The ELM burn-through simulations have the same MHD parameters as the ELM simulations without neutrals except for the following: $\kappa_{i,\perp} = \kappa_{e,\perp} = 3.7 \times 10^{-8}$ `kg.m`$^{-1}$`.s`$^{-1}$ at the pedestal top; in the core the parallel heat transport coefficients are $\kappa_{i,\parallel} = 3.7$ `kg.m`$^{-1}$`.s`$^{-1}$, $\kappa_{e,\parallel} = 1.5 \times 10^2$ `kg.m`$^{-1}$`.s`$^{-1}$. The reflective coefficient is set to 95% and $S_n = 0$.

The flux contours and electron temperature and neutral density in the divertor chamber are shown in the poloidal plane at a final time step running only with $n = 0$ at 8.5 `ms` (Fig. 18 a) and b)). The neutral density has increased in the divertor causing a decrease in the electron temperature close to the target to a few `eV`. After 8.5 `ms` a $n = 20$ perturbation is introduced and because the equilibrium is unstable a linear growth in the energy arises. The instability grows at a rate of 3.0×10^4 `s`$^{-1}$, eventually reaching a nonlinear stage where the ELM crash occurs at around 9.5 `ms`, after which there is a saturation phase. During the crash the ELM filamentary structures of high density erupt from the plasma edge, as seen in Fig. 18 c) and e). The filament size is relatively small due to the toroidal flow shear, which is included in the simulations. As expected, a collapse in the pressure pedestal occurs, the energy and particle pedestal losses are 10% and 17% respectively. Heat and particles are transported along the SOL to the divertor regions; a quick increase in the divertor temperature is seen 0.2 `ms` after the onset of the ELM crash, Fig. 18 e). This large flux from the ELM causes the hot plasma to burn through the neutrals front, Fig. 18 d) and f), ionising the neutrals and increasing the heat flux to the Super-X target. The peak heat flux to the target from the ELM is 0.8 `MW/m`^{2}, 0.2 `ms` after the ELM crash occurs. After the ELM, the neutral density starts to increase again due the increase in plasma density incident on the targets during the ELM. Fig. 18 g) and h) show the plasma density, divertor electron temperature and neutral density 4.2 `ms` after the start of the ELM crash. The filaments have reduced in size and the temperature in the divertor has decreased, as the neutral density has started to increase.

The evolution of the peak values of various quantities to the outer target are shown in Fig. 19, given by the red lines at 95% reflectivity, during the ELM crash from 9.5 `ms` to around 9.7 `ms` and in the nonlinear saturation phase. Fig. 19 shows, after an increase in the outer target heat flux during the ELM, a decrease of an order of magnitude occurs around 1 `ms` after the crash, following the peak in neutral density. This is not the case for the peak target heat flux observed in the MAST-U simulations of the Super-X using the JOREK model without neutrals - in that case the heat flux slowly decreases over several milliseconds. The results also show a significant reduction, by an order of magnitude, in the overall target heat flux of the Super-X in comparison to a conventional divertor configuration [38] or to MAST experimental heat fluxes, which were usually around a few-tens of `MW/m`^{2}.

The peak plasma density, shown in Fig. 19 at a reflectivity of 95%, increases during the ELM as the plasma burns through the neutrals front. The large amount of plasma density incident on the target during the ELM reflects an increased flux of neutrals by approximately a factor 2 causing a larger interaction between the plasma and the neutrals and thus the targets are cooled. The
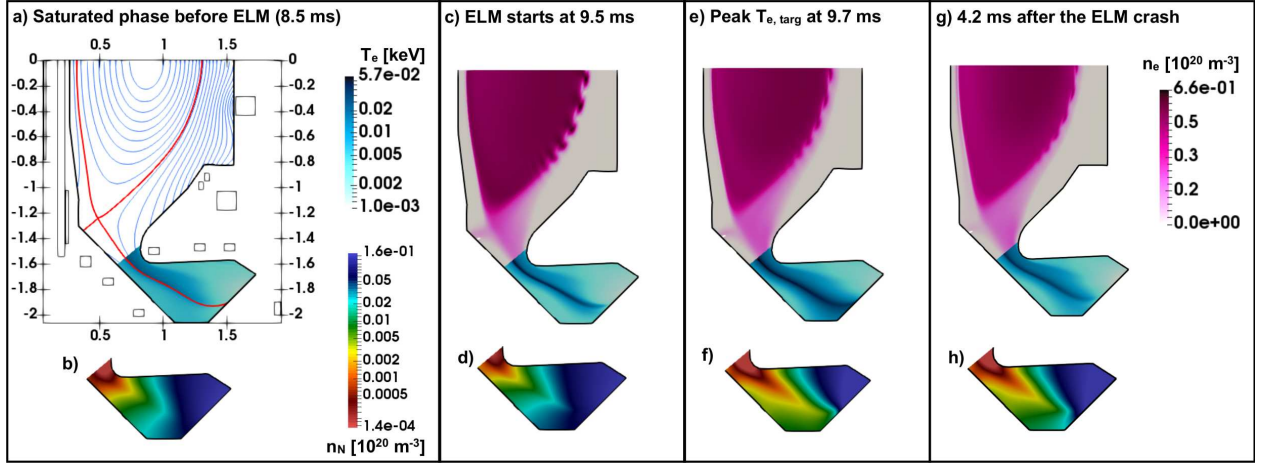
Figure 18: *Poloidal plots of a) the flux contours (blue) separatrix (red) and the divertor temperature. b) The divertor neutral density at 8.5 ms. c) The plasma density and divertor temperature and d) the neutral density at the start of the ELM. e) The plasma density and divertor temperature and f) the neutral density at 9.7 ms. g) The plasma density and divertor temperature and h) the neutral density 4.2 ms after the ELM crash. Note: the lower half of MAST-U is shown but a full tokamak grid is used in the simulations.*

initial increase in the electron temperature to 40 `eV` due to the ELM is then seen to reduce as the neutrals build-up in the divertor, as the ELM becomes less active. A few `ms` after the crash the target temperature is around the value before the ELM, showing a recovery that is shorter than a typical type-I inter-ELM phase on MAST. Around 13-14 `ms` into the simulation (approximately 4 `ms` after the ELM crash) the peak electron temperature at the target is around 5 `eV` and the ionisation front has started to move upstream from the target, suggesting a transition back to a detached state after the ELM. In the saturation phase, oscillations occur in the plasma density, and to a lesser extent the temperature and neutral density. These oscillations are related to the filaments moving into the SOL and travelling to the divertor. There is increased plasma density onto the targets, which causes an oscillation in the peak neutral density as neutrals are reflected from the wall, which are then ionised as the fluxes from the next filament arrive in the divertor.

B.1   Reflectivity scan

An initial test to explore the role of neutrals in the Super-X divertor during an ELM is conducted by altering the reflectivity coefficient, as ξ_{re} is decreased less neutrals will be present in the divertor. Recall that, the previous simulations had a reflection coefficient set to 95%. In order to have a high neutral density in the divertor the reflectivity remains the same until the perturbation ($n = 20$) is introduced. A scan of ξ_{re}, decreasing from 95% to 75%, 50% and 25%, is conducted during the ELM simulation and a plot of the evolution of the peak target values comparing the reflective coefficient is produced, given in Fig. 19. The ELM crash is observed to start earlier for lower reflectivity, indicating the growth rate of the instability decreases with increasing neutrals in the simulation domain.

Fig. 19 shows that as the reflectivity is decreased, the neutral density in the divertor decreases,

as expected. During the ELM crash the lower reflectivity leads to similar peak heat fluxes to the outer target. The plasma density increases with increasing neutral density as the neutral-plasma interactions play a role. The peak target electron temperature increases during the ELM and remains high for the reduced reflectivity cases. There is no recovery to pre-ELM conditions for the electron temperature, after the ELM crash, for the cases with lower neutral density in the divertor; in comparison to the case with $\xi_{re} = 95\%$.
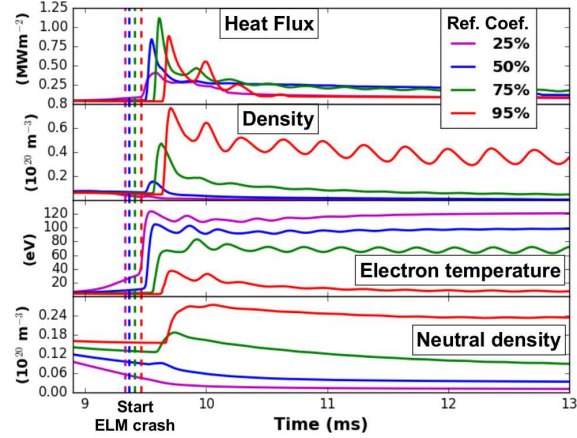

Figure 19: *Evolution of peak outer target values for varying reflective coefficient starting at a reflectivity of 95% (red lines) and decreasing. The recovery to pre-ELM conditions is only observed at high reflectivity.*